INTERNATIONAL JOURNAL OF ROBUST AND NONLINEAR CONTROL
Int. J. Robust Nonlinear Control (2008)
Published online in Wiley InterScience (www.interscience.wiley.com). DOI: 10.1002/rnc.1299

Stability- and performance-robustness tradeoffs: MIMO mixed-μ *vs* complex-μ design

J. F. Vasconcelos[1,*,†], M. Athans[1,‡], S. Fekri[1,2,§], C. Silvestre[1] and P. Oliveira[1]

[1]*Institute for Systems and Robotics* (*ISR*), *Instituto Superior Técnico* (*IST*), *Lisbon*, *Portugal*
[2]*Department of Engineering*, *Control & Instrumentation Research Laboratory*, *University of Leicester*, *Leicester LE1 7RH*, *U.K.*

SUMMARY

We present a non-trivial case study designed to highlight some of the practical issues that arise when using mixed-μ or complex-μ robust synthesis methodologies. By considering a multi-input multi-output three-cart mass–spring–dashpot (MSD) with uncertain parameters and dynamics, it is demonstrated that optimized performance (disturbance-rejection) is reduced as the level of uncertainty in one or two real parameters is increased. Comparisons are made (a) in the frequency domain, (b) by RMS values of key signals and (c) in time-domain simulations. The mixed-μ controllers designed are shown to yield superior performance as compared with the classical complex-μ design. The singular value decomposition analysis shows the directionality changes resulting from different uncertainty levels and from the use of different frequency weights. The nominal and marginal stability regions of the closed-loop system are studied and discussed, illustrating how stability margins can be extended at the cost of reducing performance.

Received 27 September 2006; Revised 26 June 2007; Accepted 20 November 2007

KEY WORDS: robust feedback control; robust mixed μ-synthesis; multivariable control systems; uncertain systems

1. INTRODUCTION

All linear time-invariant (LTI) models of real dynamic systems are subject to uncertainty. For each LTI model, we must take into account both unmodeled dynamics and uncertain real parameters, as well as the characteristics of unmeasurable exogenous plant disturbances and sensor noises. The

*Correspondence to: J. F. Vasconcelos, Institute for Systems and Robotics (ISR), Instituto Superior Técnico (IST), Av. Rovisco Pais, No. 1 Torre Norte, 8th andar-sala 8.11, 1049-001 Lisbon, Portugal.
†E-mail: jfvasconcelos@isr.ist.utl.pt
‡Professor of EECS (emeritus), M.I.T., U.S.A.
§Research Associate.

Contract/grant sponsor: Fundação para a Ciência e a Tecnologia
Contract/grant sponsor: Portuguese FCT POCTI programme; contract/grant number: SFRH/BD/18954/2004

design of a multi-input multi-output (MIMO) dynamic compensator, and of the resulting robust feedback control system, must possess guarantees of both stability- and performance-robustness with respect to the explicit performance specifications posed by the control system designer.

Fortunately, in the past decade or so, the mixed-μ design methodology [1, 2] and MATLAB software [3], utilizing the so-called D,G-K iteration, have been developed that can indeed be used to design robust MIMO feedback control systems with the requisite stability- and performance-robustness guarantees. However, there is a scarcity of detailed complex MIMO numerical studies that demonstrate the very important tradeoffs between performance and uncertainty. One of the possible reasons is that the current commercial version of the Robust Toolbox [3] in MATLAB does not fully implement the complete mixed-μ compensator design process; it uses the complex-μ and D-K iteration to design the robust compensators.

In this paper, we use a two-input two-output (TITO) mass–spring–dashpot (MSD) test example to illustrate these key performance *vs* uncertainty tradeoffs. This system may appear very simple and academic; however, it has been widely adopted in benchmark problems to highlight issues in robust control design, see [4] and references therein for a list of robust control studies using the MSD framework. The MSD dynamics are commonly used in seismic and vibration models [5–9], automotive suspension systems [10–13], flexible space structures [14–19], among others.

We have used a 'beta' version of the mixed-μ software (provided to us by Prof. Gary Balas of the University of Minnesota), which fully implements the mixed-μ D,G-K iteration leading to the best possible robust compensator. The problem of synthesizing a controller with existing control theory and computational tools, which is (optimally) robust to structured mixed uncertainty is very difficult, since the formulated D,G-K optimization problem is not convex. Because of this non-convexity, in our studies, we used a variety of initial conditions in order to avoid finding a local minimum. The complex-μ synthesis procedure, however, has been successfully applied to a large number of engineering problems (see, for example, [15]). The mixed-μ synthesis problem extends the above procedure to the mixed real/complex uncertainties case, by exploiting some new analysis tools recently developed for the mixed-μ upper bound [20].

Loosely speaking, the mixed-μ compensator design process 'detunes' an optimal $\mathscr{H}_\infty$ compensator, designed for the nominal plant, to hedge for the uncertain real parameters and the inevitable unmodeled dynamics. *The greater the parametric uncertainty, the smaller the guaranteed performance*. In this study, we shall quantify the deterioration of disturbance-rejection as the parametric uncertainty increases. Of course, since we deal with a MIMO design, 'directional properties' quantified by the singular value decomposition (SVD) are also important, which illustrate the strong interactions of the subsystems. A similar study [21] examined similar tradeoffs for a simpler single-input single-output MSD example.

In summary, the purpose of this quasi-tutorial paper is to provide guidance for analysis and concrete results related to the performance tradeoffs that are always present in MIMO feedback designs with the guaranteed stability- and performance-robustness. In particular, we discuss and evaluate the following key engineering design issues:

1. Com pensators that are designed with the current commercial version of the MATLAB Robust Toolbox [3], which employs the (complex-μ) D-K iteration for compensator design, are quite conservative and yield inferior disturbance-rejection performance compared with the compensators designed by the mixed-μ software that implements the full D,G-K iteration.
2. In robust MIMO feedback designs, for fixed performance weights, changes in the level of uncertainty associated with the real parameters can have a significant impact upon the

DOI: 10.1002/rnc

'directional properties' of the closed-loop system. Of course, these can be analyzed and evaluated by the SVD methodology.

3. In robust MIMO feedback designs with fixed uncertainty for the real parameters, designer-imposed preferences for relative performance associated with different signals will also have a significant impact upon the 'directional properties' of the closed-loop system. Again, these can be analyzed and evaluated by the SVD methodology.
4. Examine and determine the actual closed-loop stability regions for different types of 'legal' unmodeled dynamics. These can lead to some unexpected behavior.

This paper is organized as follows. In Section 2, we discuss the MSD dynamics, its uncertain real parameters, unmodeled dynamics and present the open-loop frequency-domain analysis. Section 3 presents the performance-robustness specifications for controller synthesis, modeled using frequency-domain weights, and describes the search method to optimize performance given the specifications. We define two cases, one involving a single uncertain parameter, a spring stiffness, and another that, in addition, involves an uncertain mass. In Section 4, we discuss the characteristics of the robust compensators, obtained by the mixed-μ method, in terms of performance. The performance deterioration when we add another uncertain real parameter is quantified by the performance weights, disturbance-rejection and output RMS tables. The conservativeness of the compensator designed by the complex-μ method that uses only the D-K iteration with respect to that obtained by the D,G-K iteration is also demonstrated. Section 5 presents the frequency-domain analysis of the robust compensators. The tradeoffs in terms of disturbance-rejection SVD plots are presented and the changes in the directionality of the system obtained by varying the performance weights are discussed. In Section 6, we present time transients that illustrate the deterioration in disturbance-rejection as the parametric uncertainty increases. In Section 7, we study how the actual closed-loop stability regions change as a function of using different 'legal' unmodeled dynamics and discuss the resultant changes in disturbance-rejection in the frequency domain. Section 8 presents some brief conclusions.

2. PLANT MODEL

In this work, the MSD system depicted in Figure 1 is analyzed. The nominal system is composed by three masses, denoted by m_1, m_2 and m_3, interconnected by elastic springs and dashpots elements, whose stiffness and damping coefficients are denoted by k_1, k_2, k_3 and b_1, b_2, b_3, respectively.

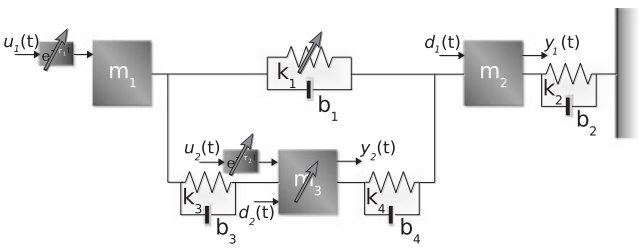

Figure 1. The two-input two-output mass–spring–dashpot (MSD) system.

DOI: 10.1002/rnc

The control inputs u_1 and u_2 are applied to masses m_1 and m_3, respectively, and are affected by unmodeled actuator dynamics, which (for the sake of exposition) we approximate by an unknown bounded pure time delay in each control channel.

Position sensors y_1 and y_2, corrupted by additive measurement noises θ_1 and θ_2, are located on masses m_2 and m_3. The performance outputs z_1 and z_2 are defined as the positions of masses m_2 and m_3, and the control objective is to minimize their displacements from their equilibrium positions, i.e. disturbance-rejection. From the system configuration, it is immediate that control u_1 is non-collocated because the performance specifications are imposed on z_1. The two disturbance forces d_1 and d_2 act on the same masses where the performance outputs are defined.

2.1. System dynamics

Based on Newton's laws, the MSD plant dynamics are derived to yield

$$\begin{aligned}
\dot{x}_1(t) &= v_1(t)\\
\dot{x}_2(t) &= v_2(t)\\
\dot{x}_3(t) &= v_3(t)\\
\dot{v}_1(t) &= -\frac{k_1+k_3}{m_1}x_1(t)+\frac{k_1}{m_1}x_2(t)+\frac{k_3}{m_1}x_3(t)-\frac{b_1+b_3}{m_1}\dot{x}_1(t)\\
&\quad +\frac{b_1}{m_1}\dot{x}_2(t)+\frac{b_3}{m_1}\dot{x}_3(t)+\frac{1}{m_1}u_1(t)\\
\dot{v}_2(t) &= \frac{k_1}{m_2}x_1(t)-\frac{k_1+k_2+k_4}{m_2}x_2(t)+\frac{k_4}{m_2}x_3(t)+\frac{b_1}{m_2}\dot{x}_1(t)\\
&\quad -\frac{b_1+b_2+b_4}{m_2}\dot{x}_2(t)+\frac{b_4}{m_2}\dot{x}_3(t)+\frac{1}{m_2}d_1(t)\\
\dot{v}_3(t) &= \frac{k_3}{m_3}x_1(t)+\frac{k_4}{m_3}x_2(t)-\frac{k_3+k_4}{m_3}x_3(t)+\frac{b_3}{m_3}\dot{x}_1(t)\\
&\quad +\frac{b_4}{m_3}\dot{x}_2(t)-\frac{b_3+b_4}{m_3}\dot{x}_3(t)+\frac{1}{m_3}u_2(t)+\frac{1}{m_3}d_2(t)
\end{aligned} \tag{1}$$

where m_i, x_i and v_i are the mass, position and velocity of mass m_i, indexed by $i=1,2,3$, and u_i and d_i are the forces and disturbances acting on the system, respectively.

The state performance outputs are defined for states $x_2(t)$ and $x_3(t)$, and the state and control performance outputs specification are defined using frequency weights

$$\mathbf{z}(s)=\begin{bmatrix}x_2(s)\\ x_3(s)\end{bmatrix},\quad \mathbf{z}_{px}(s)=\mathbf{W}_{px}(s)\mathbf{z}(s),\quad \mathbf{z}_{pu}(s)=\mathbf{W}_{pu}(s)\begin{bmatrix}u_1(s)\\ u_2(s)\end{bmatrix} \tag{2}$$

where $\mathbf{z}(s)$ denotes the states associated with the performance outputs, $\mathbf{z}_{px}(s)$ and $\mathbf{z}_{pu}(s)$ are weighted performance outputs, and $\mathbf{W}_{px}(s)$ and $\mathbf{W}_{pu}(s)$ are frequency-dependent performance weights (which will be defined in the sequel). The performance state variables are monitored by

DOI: 10.1002/rnc

position sensors corrupted by additive noise

$$\mathbf{y}(t)=\mathbf{z}(t)+\begin{bmatrix}\theta_{w1}(t)\\ \theta_{w2}(t)\end{bmatrix}$$

and $\theta_w(t)$ is the measurement noise.

The augmented state model is straightforward to obtain

$$\begin{aligned}\dot{\mathbf{x}}(t)&=\mathbf{A}\mathbf{x}(t)+\mathbf{B}_1\mathbf{w}(t)+\mathbf{B}_2\mathbf{u}(t)\\ \mathbf{z}_p(t)&=\mathbf{C}_1\mathbf{x}(t)+\mathbf{D}_{12}\mathbf{u}(t)\\ \mathbf{y}(t)&=\mathbf{C}_2\mathbf{x}(t)+\mathbf{D}_{21}\mathbf{w}(t)+\mathbf{D}_{22}\mathbf{u}(t)\end{aligned} \tag{3}$$

where the state variables $\mathbf{x}(t)$, generalized noise $\mathbf{w}(t)$, control $\mathbf{u}(t)$, performance vector $\mathbf{z}_p(t)$ and measurements $\mathbf{y}(t)$ are given by

$$\begin{aligned}&\mathbf{x}(t)=[x_1(t)\ \ x_2(t)\ \ x_3(t)\ \ v_1(t)\ \ v_2(t)\ \ v_3(t)]^{\mathrm{T}},\quad \mathbf{z}_p(t)=[\mathbf{z}_{px}(t)^{\mathrm{T}}\ \ \mathbf{z}_{pu}(t)^{\mathrm{T}}]^{\mathrm{T}}\\ &\mathbf{w}(t)=[d_1(t)\ \ d_2(t)\ \ \theta_{w1}(t)\ \ \theta_{w2}(t)]^{\mathrm{T}},\quad \mathbf{u}(t)=[u_1(t)\ \ u_2(t)]^{\mathrm{T}}\end{aligned} \tag{4}$$

The state dynamics matrix $\mathbf{A}$ is constant and described by

$$\mathbf{A}=\begin{bmatrix}\mathbf{0} & \mathbf{I}_{3\times 3}\\ \mathbf{A}_{21} & \mathbf{A}_{22}\end{bmatrix} \tag{5}$$

where submatrices $\mathbf{A}_{21}$ and $\mathbf{A}_{22}$ are related to the stiffness and damping coefficients, k_i and b_i, respectively, and are given by

$$\begin{aligned}\mathbf{A}_{21}&=\begin{bmatrix}-\dfrac{k_1+k_3}{m_1} & \dfrac{k_1}{m_1} & \dfrac{k_3}{m_1}\\ \dfrac{k_1}{m_2} & -\dfrac{k_1+k_2+k_4}{m_2} & \dfrac{k_4}{m_2}\\ \dfrac{k_3}{m_3} & \dfrac{k_4}{m_3} & -\dfrac{k_3+k_4}{m_3}\end{bmatrix}\\ \mathbf{A}_{22}&=\begin{bmatrix}-\dfrac{b_1+b_3}{m_1} & \dfrac{b_1}{m_1} & \dfrac{b_3}{m_1}\\ \dfrac{b_1}{m_2} & -\dfrac{b_1+b_2+b_4}{m_2} & \dfrac{b_4}{m_2}\\ \dfrac{b_3}{m_3} & \dfrac{b_4}{m_3} & -\dfrac{b_3+b_4}{m_3}\end{bmatrix}\end{aligned} \tag{6}$$

DOI: 10.1002/rnc

The state model matrices are constant and given by

$$\mathbf{B}_1 = \begin{bmatrix} \mathbf{0}_{3\times 2} & \mathbf{0}_{3\times 2} \\ \begin{matrix} 0 & 0 \\ \frac{1}{m_2} & 0 \\ 0 & \frac{1}{m_3} \end{matrix} & \end{bmatrix}, \quad \mathbf{B}_2 = \begin{bmatrix} \mathbf{0}_{3\times 2} \\ \begin{matrix} \frac{1}{m_1} & 0 \\ 0 & 0 \\ 0 & \frac{1}{m_3} \end{matrix} \end{bmatrix}$$
$$\mathbf{C}_1 = \begin{bmatrix} 0 & 1 & 0 & \\ 0 & 0 & 1 & \mathbf{0}_{2\times 3} \end{bmatrix}, \quad \mathbf{D}_{12} = \mathbf{0}_{2\times 2} \tag{7}$$
$$\mathbf{C}_2 = \mathbf{C}_1, \quad \mathbf{D}_{21} = [\mathbf{0}_{2\times 2} \ \mathbf{I}_{2\times 2}], \quad \mathbf{D}_{22} = \mathbf{0}_{2\times 2}$$

For this study, the known physical parameters are always fixed to the following values:

$$\begin{aligned} &m_1 = m_2 = 1\,\text{kg} \\ &b_1 = b_2 = b_3 = b_4 = 0.05\,\text{Ns/m} \\ &k_2 = 0.15\,\text{N/m}, \quad k_3 = 1.00\,\text{N/m}, \quad k_4 = 0.20\,\text{N/m} \end{aligned} \tag{8}$$

2.2. Stability robustness

The non-ideal characteristics of the plant are described in order to synthesize a controller that is robustly stable for a set of legal uncertainties and disturbances.

As shown in Figure 1, the plant includes two actuator unmodeled dynamics described by the uncertain value in the control time delay, given by the delay times τ_1 and τ_2, and two uncertain real parameters associated with the mass m_3 and the elastic coefficient k_1 values. These are modeled according to the mixed μ-synthesis framework, using either structured or unstructured uncertainty models.

2.2.1. Real parameter uncertainty. The real uncertain parameters k_1 and m_3 are described by

$$\begin{aligned} k_1 &= \bar{k}_1 + \delta_{k_1}\tilde{k}_1 \\ m_3 &= \bar{m}_3 + \delta_{m_3}\tilde{m}_3 \end{aligned} \tag{9}$$

where $\bar{k}_1$ and $\bar{m}_3$ are the nominal values, $\tilde{k}_1$ and $\tilde{m}_3$ are the uncertainty ranges and the variables $\delta_{k_1} \in \mathbb{R}$ and $\delta_{m_3} \in \mathbb{R}$ determine the structured uncertainties values and satisfy $\|\delta_{k_1}\| \leqslant 1$ and $\|\delta_{m_3}\| \leqslant 1$.

Rewriting the velocity dynamics (1) to show the elastic and damping coefficients, and omitting the dependency on time for the sake of simplicity

$$\begin{aligned} \dot{v}_1 &= \frac{1}{m_1}[k_1(x_2 - x_1) + k_3(x_3 - x_1) + b_1(\dot{x}_2 - \dot{x}_1) + b_3(\dot{x}_3 - \dot{x}_1) + u_1] \\ \dot{v}_2 &= \frac{1}{m_2}[k_1(x_1 - x_2) + k_2(-x_2) + k_4(x_3 - x_2) + b_1(\dot{x}_1 - \dot{x}_2) + b_2(-\dot{x}_2) + b_4(\dot{x}_3 - \dot{x}_2) + d_1] \\ \dot{v}_3 &= \frac{1}{m_3}[k_3(x_1 - x_3) + k_4(x_2 - x_3) + b_3(\dot{x}_1 - \dot{x}_3) + b_4(\dot{x}_2 - \dot{x}_3) + u_2 + d_2] \end{aligned} \tag{10}$$

DOI: 10.1002/rnc

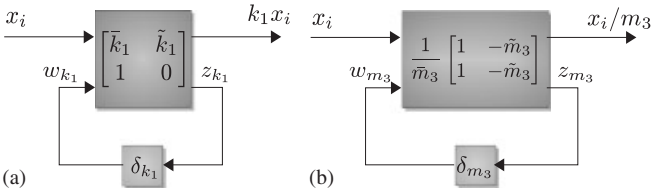

Figure 2. Structured uncertainties lower loop LFTs: (a) spring stiffness k_1 and (b) mass m_3.

it follows that the k_1 parameter appears in multiplicative form, while the m_3 uncertainty occurs in the quotient form $1/m_3$.

For the mixed-μ synthesis modeling, the real uncertainties k_1 and $1/m_3$ are regarded as scalar gain blocks, hence, described by the lower-loop LFT transfer function [3] depicted in Figure 2 and given by

$$\begin{aligned} k_1 &= F_{\mathrm{L}}\left(\begin{bmatrix} \bar{k}_1 & \tilde{k}_1 \\ 1 & 0 \end{bmatrix}, \delta_{k_1}\right) \\ \frac{1}{m_3} &= F_{\mathrm{L}}\left(\frac{1}{\bar{m}_3}\begin{bmatrix} 1 & -\tilde{m}_3 \\ 1 & -\tilde{m}_3 \end{bmatrix}, \delta_{m_3}\right) \end{aligned} \tag{11}$$

The real uncertain parameters values are

$$\begin{aligned} k_1 \in [0.25 \;\; 1.75]\,\mathrm{N/m} &\longrightarrow \bar{k}_1 = 1\,\mathrm{N/m}, \quad \tilde{k}_1 = 0.75\,\mathrm{N/m} \\ m_3 \in [0.20 \;\; 1.80]\,\mathrm{kg} &\longrightarrow \bar{m}_3 = 1\,\mathrm{kg}, \quad \tilde{m}_3 = 0.8\,\mathrm{kg} \end{aligned} \tag{12}$$

2.2.2. Unmodeled dynamics. The uncertain control actuators, representing unmodeled dynamics, are approximated by pure time delays, which are infinite-dimensional systems, so they cannot be modeled by a finite number of state variables. Assuming that the time delays are neglected, the resulting multiplicative error is

$$e_M(s) = \mathrm{e}^{-s\tau} - 1 \tag{13}$$

The multiplicative error magnitude can be approximated by an upper bound high-pass transfer function $W_{\tau i}(s)$ with a pole placed near the frequency $\omega = \pi/\tau$. For the μ-synthesis methodology, the magnitude and phase of the transfer function $W_{\tau i}(s)$ are shaped by a delta block $\Delta_{\tau i}(s) \in \mathbb{C}$ that satisfies $\|\Delta_{\tau i}(s)\|_\infty \leqslant 1$, which introduces a phase uncertainty in the range of $\pm 180°$. The corresponding block diagram is shown in Figure 3.

The control channel time-delay upper bounds are

$$\tau_i \leqslant 0.03\,\mathrm{s}, \quad i = 1, 2 \tag{14}$$

hence, the $W_{\tau i}(s)$ transfer function pole is set near the maximum time-delay frequency

$$\mathbf{W}_{\tau 1}(s) = \mathbf{W}_{\tau 2}(s) = 2.1\frac{s}{s+40} \tag{15}$$

DOI: 10.1002/rnc

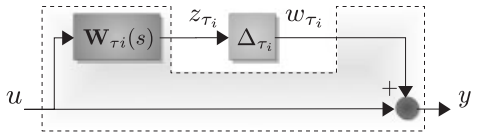

Figure 3. Time-delay error model block diagram.

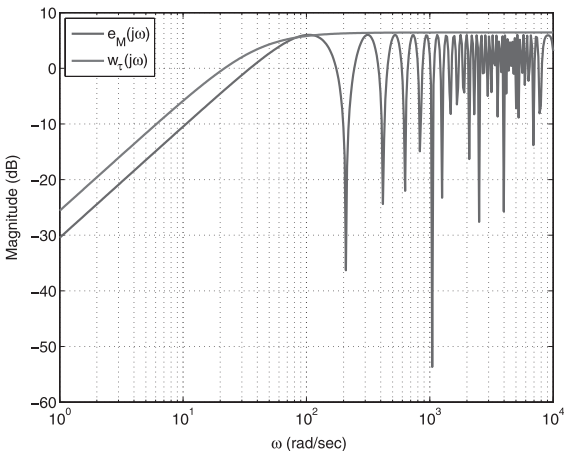

Figure 4. $e_M(s)$ upper bound, $\tau_i = 0.03\,\mathrm{s}$, see Equation (15).

and the gain adjusts the upper bound magnitude to the $e_M(s)$ transfer function, as shown in Figure 4. The frequency weight block is defined as

$$\begin{aligned} \mathbf{z}_\tau(s) &= \mathbf{W}_\tau(s)\mathbf{u}(s) \\ \mathbf{W}_\tau(s) &= \begin{bmatrix} \mathbf{W}_{\tau 1}(s) & 0 \\ 0 & \mathbf{W}_{\tau 2}(s) \end{bmatrix} \end{aligned} \tag{16}$$

The magnitudes of the transfer functions in (15) *vs* frequency, shown in Figure 4, define a class of 'legal' complex-valued unmodeled dynamics. For the purposes of stability- and performance-robustness, any complex-valued uncertainty bounded by the magnitudes of (15) represents a 'legal' set of unmodeled dynamics. This issue will be examined further in Section 7.

2.2.3. Plant disturbances. The plant disturbances are modeled as low-frequency colored noise generated by a pre-whitening process

$$\begin{aligned} \mathbf{d}(s) &= \mathbf{W}_d(s)\boldsymbol{\xi}(s) \\ \mathbf{W}_d(s) &= \frac{\alpha}{s+\alpha}\mathbf{I}_{2\times 2} \end{aligned} \tag{17}$$

where $\alpha = 2\,\mathrm{rad/s}$ is the corner frequency and $\xi(s)$ is assumed to be a zero-mean, Gaussian white noise, with unit intensity $\Xi = \mathbf{I}_{2\times 2}$. This will allow us to carry out RMS tradeoffs in the sequel.

DOI: 10.1002/rnc

The measurement noise $\boldsymbol{\theta}_w(t)$ is assumed to be a zero-mean, Gaussian white noise given by

$$\boldsymbol{\theta}_w(s) = \mathbf{W}_\theta(s)\boldsymbol{\theta}(s)$$

$$\mathbf{W}_\theta(s) = \begin{bmatrix} \Theta_{11}^{1/2} & 0 \\ 0 & \Theta_{22}^{1/2} \end{bmatrix} \tag{18}$$

where $\Theta_{11} = \Theta_{22} = 10^{-6}$ and $\boldsymbol{\theta}(s)$ is a zero-mean, Gaussian white noise, with unit intensity.

2.3. *Frequency-domain analysis*

The maximum and minimum singular values of the disturbance and control to state performance transfer functions, $T_{dz}(s)$ and $T_{uz}(s)$, respectively, are presented in Figures 5 and 6. As expected by the physics of a MSD system, increasing the spring stiffness k_1 or decreasing the mass coefficient m_3 will increase the system's natural frequencies, and *vice versa*. Also note that changes in the mass and spring values will change the 'coupling' between the two subsystems. Of course, in this multivariable setting the coupling can be understood by the SVD methodology.

Mass 3 value does not influence the disturbance to performance transfer function $T_{dz}(s)$ MIMO zeros, located at $z_{1,2} = -0.05 \pm j1.41$. By the definition of transfer function zero, when the $\mathbf{d}(s)$ inputs and the initial conditions of the plant states correspond to the $T_{dz}(s)$ zeros, mass 3 will remain in a stationary position. Thus, using physical intuition it is easy to see that the value of m_3 does not influence the zero location. On the contrary, the stiffness coefficient k_1 influences the open-loop zeros, since it characterizes the dynamic coupling of masses 1 and 2.

The control to output transfer function $T_{uz}(s)$ has no MIMO zeros because the control $u_1(t)$ acts on mass 1 while the performance variable $z_1(t)$ is defined on mass 2, i.e. $u_1(t)$ is non-collocated. Non-collocated control problems are more difficult (due to the absence of zeros).

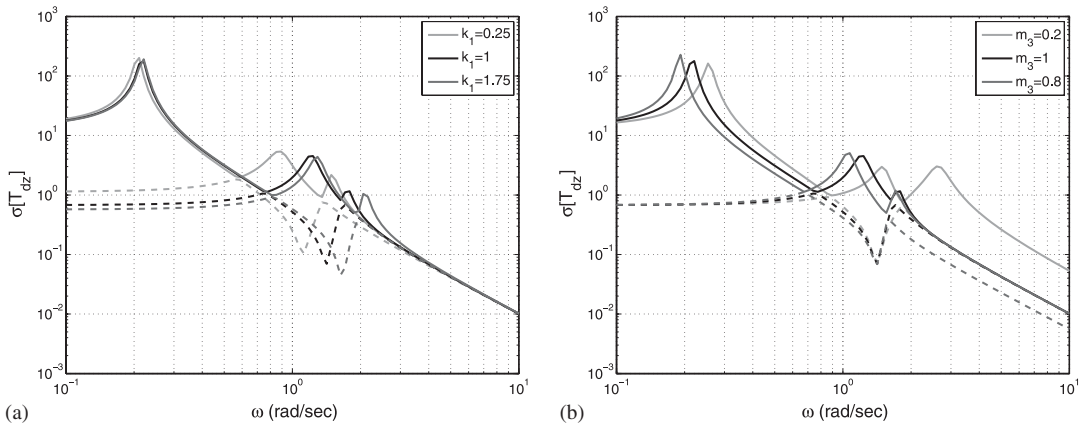

Figure 5. Open-loop disturbance d to performance output z singular values, T_{dz}: (a) varying k_1, nominal m_3 and (b) nominal k_1, varying m_3.

DOI: 10.1002/rnc

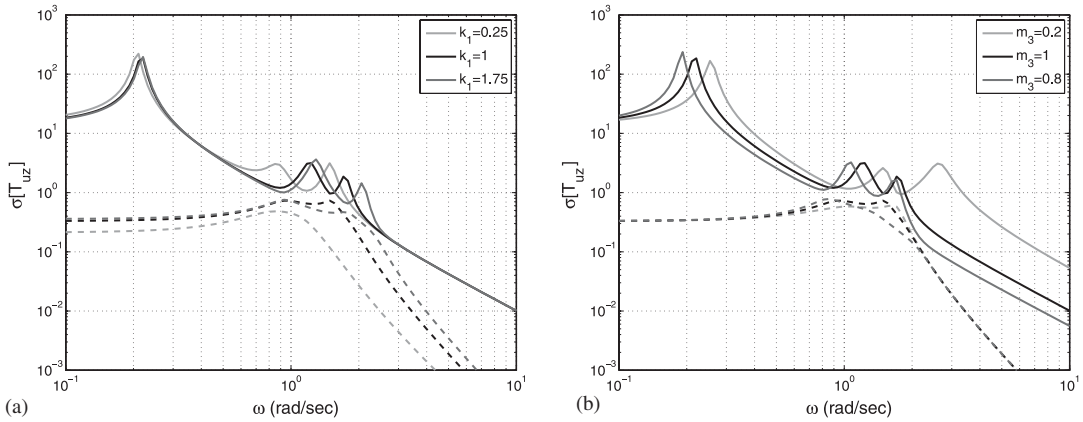

Figure 6. Open-loop control to performance output z singular values, $T_{uz}(s)$: (a) varying k_1, nominal m_3 and (b) nominal k_1, varying m_3.

More important, note that the open-loop dynamics amplify the low-frequency disturbance $\mathbf{d}(s)$, which has most of its power for $\omega<2$ rad/s as defined in (17). The controller must shape the directionality of the closed-loop system to filter out the disturbance effects in the performance vector.

3. PERFORMANCE ROBUSTNESS

The performance-robustness specifications are introduced in the generalized plant, shown in Figure 7, in the form of frequency weights. The performance outputs $\mathbf{z}_{px}(t)$ and $\mathbf{z}_{pu}(t)$ represent the state and control specifications, respectively, see (2).

The system performance weight is defined by the positions of masses 2 and 3, and implies good disturbance-rejection at the frequency range, where the disturbance $\mathbf{d}(s)$ has most of its power

$$\begin{aligned} \mathbf{z}_{px}(s) &= \mathbf{W}_{px}(s)\mathbf{z}(s) \\ \mathbf{W}_{px}(s) &= \frac{A_p\alpha}{s+\alpha}\begin{bmatrix} A_1 & 0 \\ 0 & A_2 \end{bmatrix}, \quad \alpha=2 \text{ rad/s} \end{aligned} \tag{19}$$

where the weights A_1 and A_2 shape the directionality of the system by penalizing the displacement of m_1 and m_3, respectively. The A_p weight controls the best possible disturbance-rejection and is iteratively maximized in the μ-synthesis procedure.

The larger the A_p, the better the disturbance-rejection. Also note that in (19) we use the same corner frequency α as in the disturbance dynamics (17). Thus, we are communicating to the mathematics that we are interested in superior disturbance-rejection over the same frequency range where the disturbances have most of their power.

We assume that control power is available at low frequencies but actuation is expensive at high frequencies, thereby limiting the bandwidth of the closed-loop system. Towards this end, we shall

DOI: 10.1002/rnc

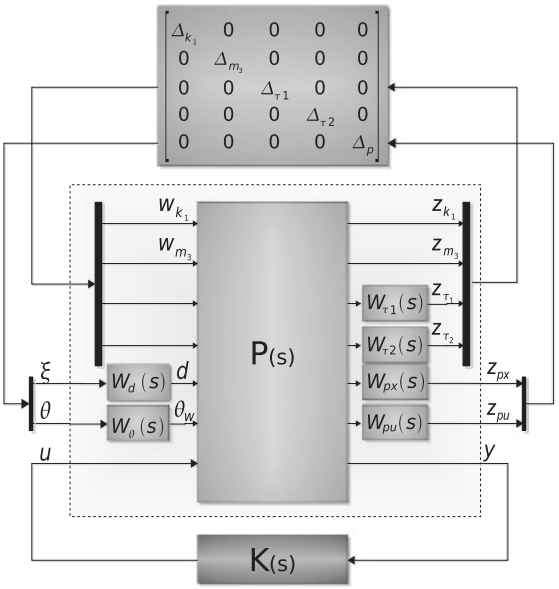

Figure 7. Generalized plant.

use the following frequency weight on the control signals:

$$\mathbf{z}_{pu}(t) = \mathbf{W}_{pu}(s)\begin{bmatrix} u_1(s) \\ u_2(s) \end{bmatrix}$$
$$\mathbf{W}_{pu}(s) = \frac{10(s+10^2)}{s+10^6}\mathbf{I}_{2\times 2} \tag{20}$$

where the Bode plot of $W_{pu}(s) := [\mathbf{W}_{pu}(s)]_{11} = [\mathbf{W}_{pu}(s)]_{22}$ is shown in Figure 8.

As described in [22], the performance-robustness specifications are satisfied by introducing an additional performance delta block $\Delta_p(s)$ in the μ-synthesis methodology.

The mixed-μ synthesis methodology is used to find the largest performance weight A_p for superior disturbance-rejection for the MSD plant. The structured singular value μ upper bound, denoted by $\bar{\mu}$, is found to monotonically increase with the performance weight A_p, as shown in Figure 9. For sufficient significant purely complex blocks, the μ value is continuous [22], which is guaranteed by the unmodeled dynamics (time delay) and performance delta blocks.

The closed-loop performance is optimized by using the bisection search method to find the largest A_p such that the norm of the smallest destabilizing structured uncertainty is greater than unity [22], i.e. $\bar{\mu}<1$. The algorithm parameters are:

- $\underline{A}_p, \bar{A}_p$—Lower and upper bounds of the A_p search interval.
- ε_A—Maximum length of the interval $[\underline{A}_p \;\; \bar{A}_p]$, i.e. the accuracy of the optimal A_p.
- `MU_ITER`—Number of D-K/D,G-K iterations to determine an upper bound for μ.
- `MAX_TRIES`—Number of different initializations for the D-K/D,G-K iterations.

DOI: 10.1002/rnc

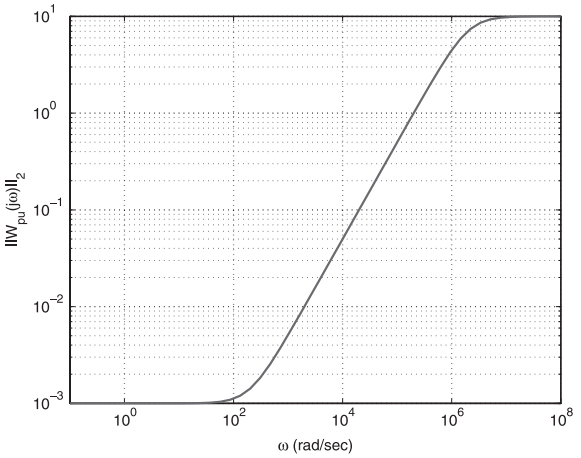

Figure 8. Control frequency-dependent weight $W_{pu}(s)$, see Equation (20).

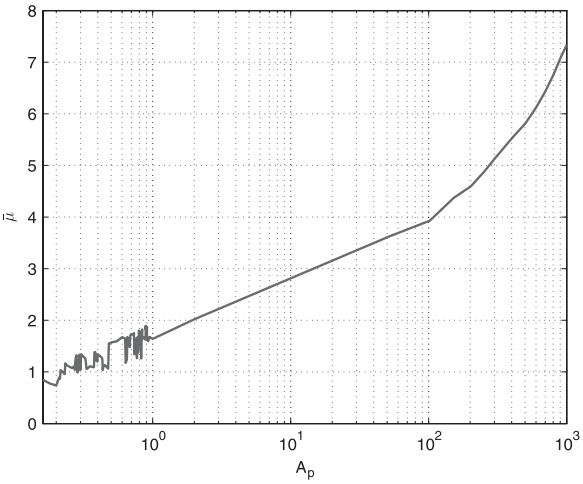

Figure 9. μ upper bound $\bar{\mu}$ *vs* performance weight A_p.

The μ-synthesis performance optimization algorithm is run as follows:

1. Make $A_p = (\bar{A}_p + \underline{A}_p)/2$ and $n_{\text{try}} = 1$.
2. Set the initial conditions using a random seed. Run `MU_ITER` D-K/D,G-K iterations.
3. Select the smallest complex-μ/mixed-μ upper bound, $\mu^* = \min\{\bar{\mu}_1, \ldots, \bar{\mu}_{\texttt{MU\_ITER}}\}$. If $\mu^* > 1$ and $n_{\text{try}} < \texttt{MAX\_TRIES}$, increment n_{try} and return to step 2.
4. If $\mu^* < 1$, set $\underline{A}_p = A_p$. Else, $\bar{A}_p = A_p$.
5. If $\bar{A}_p - \underline{A}_p < \varepsilon_A$, set $A_p = \underline{A}_p$ and $\mu = \mu^*$, STOP. Else, return to step 1.

DOI: 10.1002/rnc

The D-K and D,G-K iterations are run by the `dgit` and `dgkit` commands included in the Robust Control Toolbox of Matlab 7.1 and in the beta version software kindly provided by Prof. Gary Balas. This implementation of the D-K and D,G-K iterations leads to a robust controller [22], and an optimization algorithm (that is a modified gradient descent method) is used to compute the outputs of the D-K and D,G-K algorithms, namely, the μ bounds and the sensitivity. In this search-direction optimization method, an initial guess (search point) is selected from which the algorithm will (hopefully) converge to the desired global minima. For the purpose of this study, we have used a number of random search points and have chosen the one which achieves the lowest minimum; we assume it is the global minimum.

The iteration parameters are defined as `MU_ITER`$=40$, `MAX_TRIES`$=3$, $\varepsilon_A = 0.05$, and the maximum dynamical order of the D and G scaling matrices is defined as 60. The starting $\underline{A}_p$ and $\bar{A}_p$ parameters are defined according to the parametric uncertainty ranges $\tilde{k}_1$ and $\tilde{m}_3$.

In this study, the μ compensator properties are studied by varying the generalized plant parameters in terms of the stability- and performance-robustness specifications. We start with a single parametric uncertainty on the spring stiffness k_1 and analyze the effects of adding a second parametric uncertainty on mass m_3. Also, the parametric uncertainty ranges $\tilde{k}_1$ and $\tilde{m}_3$ are varied to quantify the effects of uncertainty on the closed-loop system performance and on its frequency-domain properties.

The directionality of the controller is also studied by varying the performance weights A_1 and A_2 in the performance output $\mathbf{z}_{px}(t)$, see (19),

- $A_1 = 1$, $A_2 = 1$ (nominal).
- $A_1 = 5$, $A_2 = 1$ (better control of mass 2 position).
- $A_1 = 1$, $A_2 = 5$ (better control of mass 3 position).

which will influence the characteristics of the controller with respect to the parametric uncertainties and change the directional properties (dynamic coupling) of the closed-loop system.

4. PERFORMANCE RESULTS

In this section, the performance obtained by the μ-synthesis methodology is discussed. The influence of the number of uncertainties, the uncertainty level and the performance weight directionality in performance-robustness is analyzed and quantified. Moreover, the robust compensators obtained by the D-K and D,G-K iterations are compared to demonstrate the importance of modeling real parametric uncertainties in the closed-loop performance and the performance advantage of the D,G-K iterative scheme.

4.1. Single parameter uncertainty

The performance results for a single uncertainty in the spring stiffness δ_{k_1}, computed for the worst-case performance disturbance, are shown in Table I using the complete mixed-μ D,G-K iteration. It is clear that smaller uncertainty ranges $\tilde{k}_1$ yield larger performance weight A_p; hence, we should expect better disturbance-rejection. The norm $\|\|$ is the maximum singular value of the disturbance-rejection at DC, i.e. $\omega = 0$ rad/s; as we shall see it remains at about the same value at low frequencies. The RMS errors assume white-noise signals as discussed in (17) and (18).

DOI: 10.1002/rnc

Table I. D,G-K iteration mixed-μ performance results (only k_1 uncertain, $A_1=1$, $A_2=1$).

$\tilde{k}_1$	A_p	$\bar{\mu}$	$\|T_{\xi z}(0)\|$	RMS(z_1)	RMS(z_2)	RMS(u_1)	RMS(u_2)
0.75	23.28	0.999	3.51×10^{-2}	1.40×10^{-2}	3.51×10^{-2}	51.61	1.94
0.50	63.79	0.997	1.44×10^{-2}	1.04×10^{-2}	2.27×10^{-2}	50.39	2.22
0.25	134.93	0.999	7.18×10^{-3}	7.80×10^{-3}	8.24×10^{-3}	85.91	1.27
≈0	223.25	0.999	4.27×10^{-3}	7.63×10^{-3}	1.22×10^{-2}	87.74	2.30

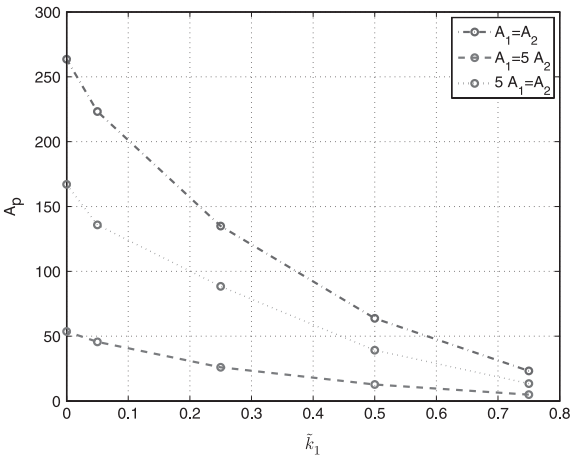

Figure 10. Performance weight A_p *vs* uncertainty range $\tilde{k}_1$ (only k_1 uncertain).

The values of the maximized performance weight A_p are not linear with respect to increasing uncertainty $\tilde{k}_1$, as shown in Figure 10. As the spring uncertainty level $\tilde{k}_1$ grows, the control problem becomes harder and A_p tends to zero, indicating inferior disturbance-rejection. The guarantee of performance robustness fades out as the plant dynamics become vaguely known, agreeing with physical intuition.

The disturbance-rejection gain for low frequencies $\|T_{\xi z_1}(0)\|$ decreases with increasing uncertainty and is about $1/A_p$, as expected. The RMS value of the performance output $\mathbf{z}(t)$ tends to decrease, reflecting better performance robustness, whereas the control RMS tends to increase due to higher compensator feedback gain for smaller uncertainties. Note that μ-synthesis is based on H_∞ control theory; hence, the H_2 norms of the performance output and the control signal are not addressed in the controller design, and the H_2 norm (i.e. RMS) trends cannot be precisely established.

The performance-robustness results for asymmetric performance weights ($A_1=5$, $A_2=1$) and ($A_2=1$, $A_2=5$) are shown in Tables II and III, respectively.

Examination of Tables I–III reveals the fact that the presence of non-collocated control makes mass 2 position harder to control; hence, the performance specification associated with $z_1(t)$ is more difficult to satisfy than that for $z_2(t)$. Consequently, the performance weight A_p is lower for $A_1=5A_2$ than for $A_2=5A_1$, while the disturbance-rejection at low frequencies $\|T_{\xi z}(0)\|$ is higher for $A_2=5A_1$ than for $A_1=5A_2$. The fact that for the same uncertainty range $\tilde{k}_1$, $\|T_{\xi z}(0)\|$ is always

DOI: 10.1002/rnc

Table II. D,G-K iteration mixed-μ performance results (only k_1 uncertain, $A_1=5, A_2=1$).

$\tilde{k}_1$	A_p	$\bar{\mu}$	$\|T_{\xi z}(0)\|$	RMS(z_1)	RMS(z_2)	RMS(u_1)	RMS(u_2)
0.75	4.93	0.999	1.01×10^{-1}	1.35×10^{-2}	7.58×10^{-2}	50.98	1.61
0.50	12.71	0.999	4.77×10^{-2}	9.56×10^{-3}	3.81×10^{-2}	80.76	1.23
0.25	26.04	0.999	2.32×10^{-2}	7.98×10^{-3}	2.35×10^{-2}	123.37	1.27
≈0	45.60	0.999	1.06×10^{-2}	7.51×10^{-3}	2.60×10^{-2}	78.51	1.94

Table III. D,G-K iteration mixed-μ performance results (only k_1 uncertain, $A_1=1, A_2=5$).

$\tilde{k}_1$	A_p	$\bar{\mu}$	$\|T_{\xi z}(0)\|$	RMS(z_1)	RMS(z_2)	RMS(u_1)	RMS(u_2)
0.75	13.43	0.999	2.22×10^{-2}	2.11×10^{-2}	2.42×10^{-2}	90.72	1.65
0.50	39.25	0.997	1.42×10^{-2}	1.31×10^{-2}	1.73×10^{-2}	63.96	2.22
0.25	88.40	0.997	8.56×10^{-3}	1.03×10^{-2}	3.66×10^{-3}	55.73	1.27
≈0	135.85	0.999	6.91×10^{-3}	1.10×10^{-2}	5.52×10^{-3}	55.32	2.25

Table IV. D,G-K iteration mixed-μ performance weight A_p (k_1, m_3 uncertain, $A_1=A_2$).

	$\tilde{k}_1$			
$\tilde{m}_3$	0.75	0.50	0.25	≈0
0.80	15.27	42.79	47.19	62.40
0.50	18.95	57.44	127.18	204.12
0.20	20.90	62.85	130.92	216.15
≈0	22.98	63.90	134.56	221.62

higher for $A_1=5A_2$ than for any of the other two cases indicates that precisely controlling the mass 2 position is a very hard control problem, and this observation is consistent with engineering intuition.

4.2. Two real parameter uncertainties

In this case, the spring stiffness k_1 and mass m_3 are both considered to be real uncertain parameters. The values of the performance weight A_p and disturbance-rejection for low-frequencies $\|T_{\xi z}(0)\|$ are illustrated in Tables IV and V, respectively.

The extra uncertainty in mass m_3 degrades the performance of the closed-loop system, as expected. Large uncertainty ranges $\tilde{k}_1$ and $\tilde{m}_3$ yield smaller values of the maximized performance weight A_p as in the single uncertainty case. Interestingly enough, the A_p values for a very small mass uncertainty range ($\bar{m}_3\approx0$) are similar to those obtained in the single parametric uncertainty case, see Tables IV and I.

The RMS values of the performance vector, presented in Tables VI and VII, tend to decrease as the uncertainties ranges $\tilde{m}_3$ and $\tilde{k}_1$ decrease. The RMS value of control $u_1(t)$ shows a tendency

DOI: 10.1002/rnc

Table V. D,G-K iteration mixed-μ disturbance-rejection $\|T_{\xi z}(0)\|$ (k_1, m_3 uncertain, $A_1 = A_2$).

	$\tilde{k}_1$			
$\tilde{m}_3$	0.75	0.50	0.25	≈ 0
0.80	6.42×10^{-2}	2.30×10^{-2}	1.78×10^{-2}	1.59×10^{-2}
0.50	4.94×10^{-2}	1.70×10^{-2}	7.71×10^{-3}	4.76×10^{-3}
0.20	4.06×10^{-2}	1.52×10^{-2}	7.41×10^{-3}	4.42×10^{-3}
≈ 0	3.61×10^{-2}	1.46×10^{-2}	7.05×10^{-3}	4.33×10^{-3}

Table VI. D,G-K iteration mixed-μ performance output RMS(z_1) (k_1, m_3 uncertain, $A_1 = A_2$).

	$\tilde{k}_1$			
$\tilde{m}_3$	0.75	0.50	0.25	≈ 0
0.80	1.84×10^{-2}	1.59×10^{-2}	1.99×10^{-2}	1.88×10^{-2}
0.50	1.72×10^{-2}	9.98×10^{-3}	8.07×10^{-3}	7.76×10^{-3}
0.20	1.83×10^{-2}	9.45×10^{-3}	7.96×10^{-3}	7.57×10^{-3}
≈ 0	1.40×10^{-2}	9.36×10^{-3}	7.88×10^{-3}	7.70×10^{-3}

Table VII. D,G-K iteration mixed-μ performance output RMS(z_2) (k_1, m_3 uncertain, $A_1 = A_2$).

	$\tilde{k}_1$			
$\tilde{m}_3$	0.75	0.50	0.25	≈ 0
0.80	5.39×10^{-2}	2.53×10^{-2}	2.20×10^{-2}	1.94×10^{-2}
0.50	4.55×10^{-2}	2.44×10^{-2}	1.48×10^{-2}	1.26×10^{-2}
0.20	3.27×10^{-2}	1.91×10^{-2}	1.29×10^{-2}	1.26×10^{-2}
≈ 0	2.47×10^{-2}	2.05×10^{-2}	1.54×10^{-2}	9.70×10^{-3}

to increase as the uncertainty decreases, see Table VIII(a). Thus, the control attains higher values for improved performance.

As shown in Table VIII(b), the RMS value of the control input $u_2(t)$ also tends to increase as $\tilde{k}_1$ decreases. But the RMS value of the control input $u_2(t)$ tends to decrease as $\tilde{m}_3$ decreases, evidencing an opposite behavior. Physically, this characteristic of the control input $u_2(t)$ is related to the fact that $u_2(t)$ is collocated with mass m_3.

As evidenced in Tables IV and V and depicted in Figure 11(a), for $A_1 = A_2$ the performance weight A_p and the low-frequency disturbance-rejection $\|T_{\xi z}(0)\|$ are more influenced by the spring stiffness uncertainty $\tilde{k}_1$ than by the mass uncertainty $\tilde{m}_3$. Physically, this reflects the importance of the uncertainty k_1 in the non-collocated control problem, where the control input $u_1(t)$'s influence on mass 2 position is channeled through the uncertain spring 1.

If the performance weights A_1 and A_2 are changed, the influence of parametric uncertainty on performance is affected. The effects of the spring uncertainty $\tilde{k}_1$ on performance are stronger for

DOI: 10.1002/rnc

Table VIII. D,G-K iteration mixed-μ control input RMS (k_1, m_3 uncertain, $A_1 = A_2$): (a) RMS (u_1) and (b) RMS (u_2).

	$\tilde{k}_1$			
$\tilde{m}_3$	0.75	0.50	0.25	≈ 0
(a) $RMS(u_1)$				
0.80	46.95	63.23	52.07	108.17
0.50	49.78	77.54	62.42	86.15
0.20	55.06	58.37	62.41	86.99
≈ 0	74.64	68.24	71.84	73.53
(b) $RMS(u_2)$				
0.80	1.37	1.51	1.71	1.47
0.50	1.74	1.76	1.86	1.93
0.20	1.68	1.67	1.70	1.98
≈ 0	1.17	1.87	2.02	2.18

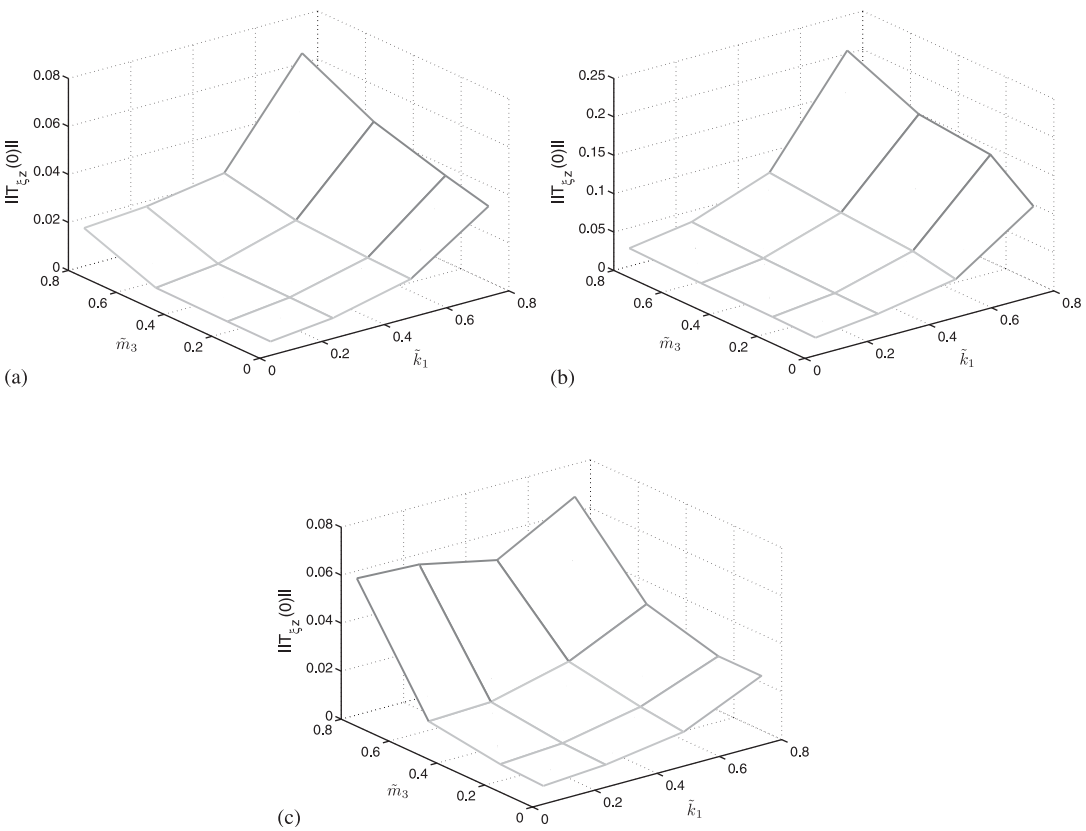

Figure 11. Disturbance-rejection $\|T_{\tilde{\xi}z}(0)\|$ *vs* uncertainty range $(\tilde{k}_1, \tilde{m}_3)$: (a) $A_1 = A_2$; (b) $A_1 = 5A_2$; and (c) $A_2 = 5A_1$.

DOI: 10.1002/rnc

Table IX. D,G-K iteration mixed-μ performance weight A_p (k_1, m_3 uncertain, $A_1 = 5A_2$).

	$\tilde{k}_1$			
$\tilde{m}_3$	0.75	0.50	0.25	≈ 0
0.80	4.28	12.43	26.07	41.67
0.50	4.71	12.96	27.01	45.81
0.20	4.74	13.01	27.06	46.37
≈ 0	4.77	13.05	27.10	46.45

Table X. D,G-K iteration mixed-μ disturbance-rejection $\|T_{\xi z}(0)\|$ (k_1, m_3 uncertain, $A_1 = 5A_2$).

	$\tilde{k}_1$			
$\tilde{m}_3$	0.75	0.50	0.25	≈ 0
0.80	2.04×10^{-1}	7.25×10^{-2}	3.56×10^{-2}	2.33×10^{-2}
0.50	1.64×10^{-1}	6.32×10^{-2}	3.13×10^{-2}	2.08×10^{-2}
0.20	1.54×10^{-1}	5.61×10^{-2}	2.88×10^{-2}	1.98×10^{-2}
≈ 0	1.13×10^{-1}	4.53×10^{-2}	2.77×10^{-2}	1.85×10^{-2}

Table XI. D,G-K iteration mixed-μ performance weight A_p (k_1, m_3 uncertain, $A_2 = 5A_1$).

	$\tilde{k}_1$			
$\tilde{m}_3$	0.75	0.50	0.25	≈ 0
0.80	4.85	11.63	13.75	15.87
0.50	9.47	30.96	64.39	84.45
0.20	13.81	41.09	90.51	135.89
≈ 0	14.63	43.02	99.26	153.03

Table XII. D,G-K iteration mixed-μ disturbance-rejection $\|T_{\xi z}(0)\|$ (k_1, m_3 uncertain, $A_2 = 5A_1$).

	$\tilde{k}_1$			
$\tilde{m}_3$	0.75	0.50	0.25	≈ 0
0.80	6.64×10^{-2}	4.87×10^{-2}	5.65×10^{-2}	5.70×10^{-2}
0.50	3.53×10^{-2}	2.02×10^{-2}	1.21×10^{-2}	1.11×10^{-2}
0.20	2.74×10^{-2}	1.50×10^{-2}	8.64×10^{-3}	6.94×10^{-3}
≈ 0	2.74×10^{-2}	1.28×10^{-2}	7.97×10^{-3}	6.14×10^{-3}

$A_1 = 5A_2$, as shown in Tables IX and X and Figure 11(b), whereas performance is more influenced by mass m_3 uncertainty for $A_2 = 5A_1$, as shown in Tables XI and XII and Figure 11(c).

Physically, the former case focuses on control of mass 2, which is performed partially through spring k_1, and the latter case concerns the control of mass 3, directly related to m_3 uncertainty.

DOI: 10.1002/rnc

Again, note that the low-frequency disturbance-rejection $\|T_{\xi z}(0)\|$ is worse for $A_1 = 5A_2$, since the control of the position of mass 2 is a more difficult problem.

Next, we designed the robust compensator using the complex-μ synthesis that uses the simpler D-K iteration, i.e. the version in the current commercially available MATLAB software [3]. This was done to expose the conservatism when one models real parameter errors with complex-valued ones and to demonstrate the degradation in disturbance-rejection. This method is used to find the best performance weight A_p such that $\bar{\mu} < 1$ for $\delta_{k_1} \in \mathbb{C}$.

The results, shown in Tables XIII and XIV, show that the D-K iteration framework is very conservative. From Tables XIII and XIV, we deduce that the mixed-μ compensator (designed by the full D,G-K iteration) yields a disturbance-rejection about three to five times better than the purely complex-μ compensator (designed by the simpler D-K iteration). This quantifies the fact that representing real parametric uncertainties by a complex unit circle is a very conservative approach. The results for the D-K and the D,G-K iterations are similar only when the uncertainty range $\tilde{k}_1$ is very small ($\tilde{k}_1 \approx 0$), which is of little interest since the parameter k_1 is known.

The results of this section have demonstrated that:

- The level of disturbance-rejection is a function of the size and number of parametric uncertainties. In general, the larger the parametric uncertainties, the worse the level of the disturbance-rejection at low frequencies.
- The compensators derived by the complex-μ D-K iterations assumptions are very conservative (by a factor of 3–5) when we have significant real parametric uncertainties. The mixed-μ, utilizing the D,G-K iteration, synthesis methodology is highly recommended for robust control synthesis with significant real parametric uncertainties, a most common occurrence.
- The directionality introduced by the performance weights A_1 and A_2 impacts the characteristics of the control design. The specific influence of a parametric uncertainty on performance depends on the performance weights directionality.

Table XIII. D-K iteration (complex-μ) *vs* D,G-K iteration (mixed-μ) performance (k_1 uncertain, $\tilde{k}_1 = 0.75$).

	D-K iteration		D,G-K iteration	
	A_p	$\|T_{\xi z}(0)\|$	A_p	$\|T_{\xi z}(0)\|$
$A_1 = 1, A_2 = 1$	5.31	0.123	23.28	3.51×10^{-2}
$A_1 = 5, A_2 = 1$	1.15	0.279	4.93	0.101
$A_1 = 1, A_2 = 5$	5.37	8.70×10^{-2}	13.43	2.22×10^{-2}

Table XIV. D-K iteration (complex-μ) *vs* D,G-K iteration (mixed-μ) performance (k_1, m_3 uncertain, $\tilde{k}_1 = 0.75$, $\tilde{m}_3 = 0.80$).

	D-K iteration		D,G-K iteration	
	A_p	$\|T_{\xi z}(0)\|$	A_p	$\|T_{\xi z}(0)\|$
$A_1 = 1, A_2 = 1$	4.28	0.204	15.27	6.42×10^{-2}
$A_1 = 5, A_2 = 1$	4.43	0.225	4.28	0.201
$A_1 = 1, A_2 = 5$	4.20	0.236	4.85	6.64×10^{-2}

DOI: 10.1002/rnc

5. FREQUENCY-DOMAIN ANALYSIS

In this section, the frequency-domain characteristics of the mixed-μ compensator are analyzed. The relationship of the frequency weights with the closed-loop transfer functions is illustrated, in particular by focusing upon the disturbance-rejection at the low-frequency region. The directionality of the system is clearly depicted in the SVD plots and in the maximum and minimum singular values ratio. The mixed- and complex-μ synthesis disturbance-rejection and compensator transfer functions are shown to demonstrate the enhanced performance robustness obtained by using the D,G-K iterations.

The disturbance to performance output maximum singular values of the closed-loop transfer function $T_{\xi z}(s)$ are depicted in Figure 12(a). In the frequency domain, the closed-loop transfer function yields good disturbance-rejection at the desired frequencies $\omega \in [0\ \ 2]\,\mathrm{rad/s}$, where $\mathbf{d}(s)$ has more power according to the performance-robustness specifications. Smaller uncertainty ranges $\tilde{k}_1$ allow for better disturbance-rejection, confirming the summary results previously shown in Table I.

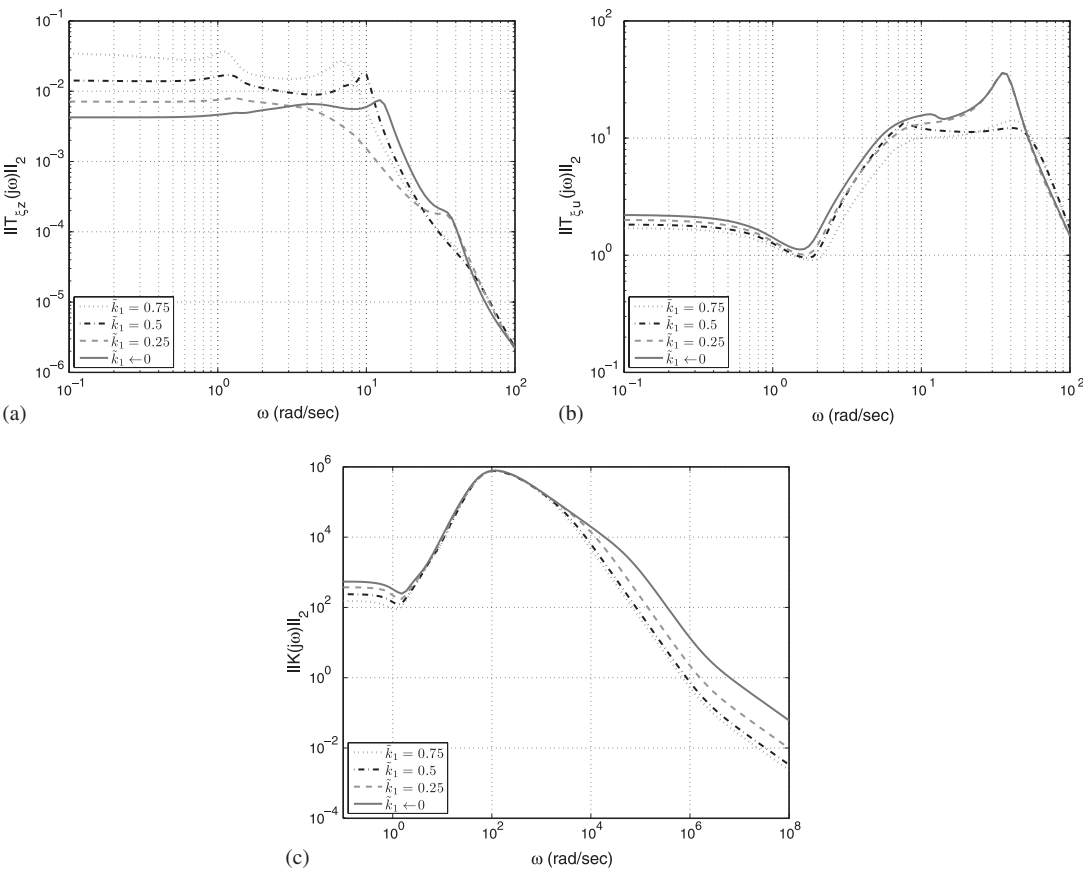

Figure 12. Maximum singular value (only k_1 uncertain, $A_1 = A_2$): (a) $T_{\xi z}(s)$; (b) $T_{\xi u}(s)$; and (c) $K(s)$.

DOI: 10.1002/rnc

Enhancing the low-frequency disturbance-rejection increases the closed-loop bandwidth; hence, performance degrades at high frequencies. Considering that the $\mathbf{d}(s)$ is modeled by low-pass frequency weights (17), the μ-synthesis methodology finds the best controller for the frequencies where the disturbance has more power. This approach eventually increases the gains at the remaining frequency regions—a fact well known in H_∞ theory [23]—but if the disturbance is correctly modeled, the additional closed-loop bandwidth does not result in actual performance degradation. Simulation results for generic disturbances that confirm this fact are presented in the following section.

The disturbance-rejection characteristics are also shown in the disturbance to control $T_{\xi u}(s)$ transfer function, see Figure 12(b). Reducing the uncertainty $\tilde{k}_1$ yields slightly larger controls at low frequencies $\omega \in [0\ \ 2]\,\text{rad/s}$.

The tradeoff between uncertainty and performance robustness is clear in the singular-value Bode plot of the compensator transfer function $K(s)$ presented in Figure 12(c). The compensator gains are larger for smaller uncertainties $\tilde{k}_1$, and according to the performance control weights $\mathbf{W}_{pu}(s)$

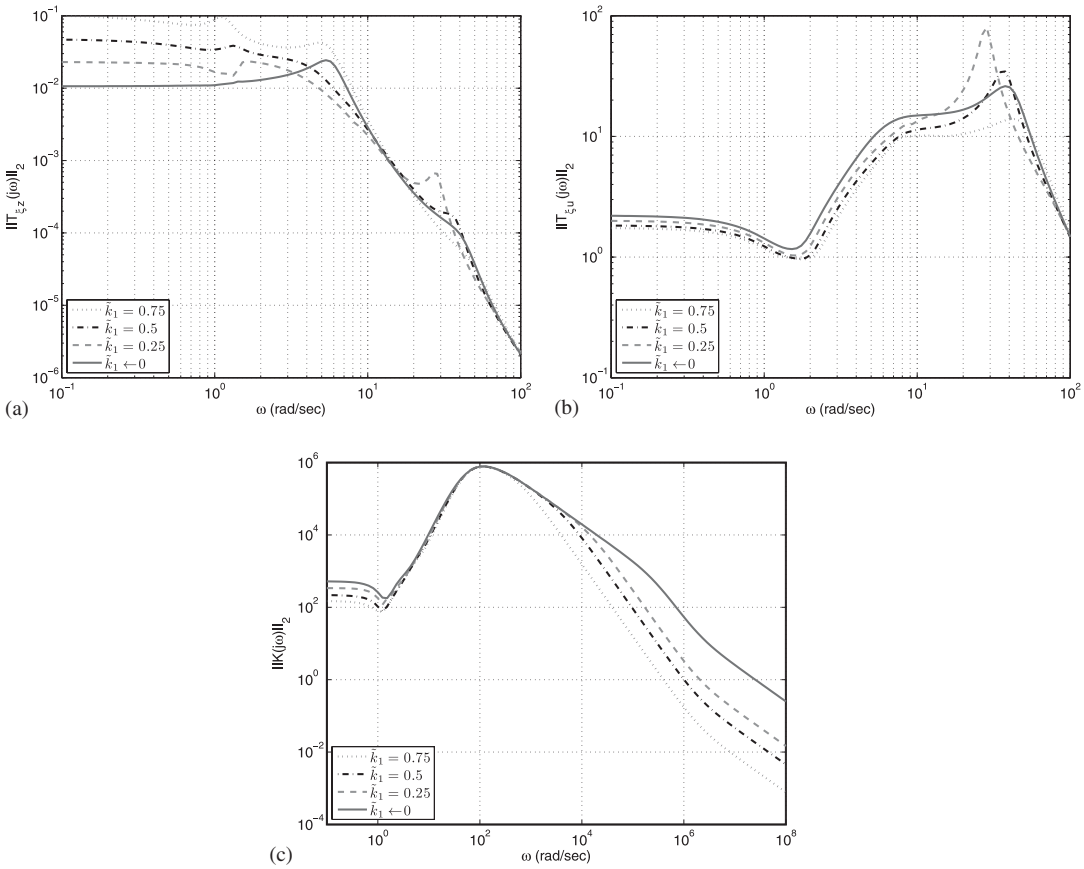

Figure 13. Maximum singular value (only k_1 uncertain, $A_1 = 5A_2$): (a) $T_{\xi z}(s)$; (b) $T_{\xi u}(s)$; and (c) $K(s)$.

DOI: 10.1002/rnc

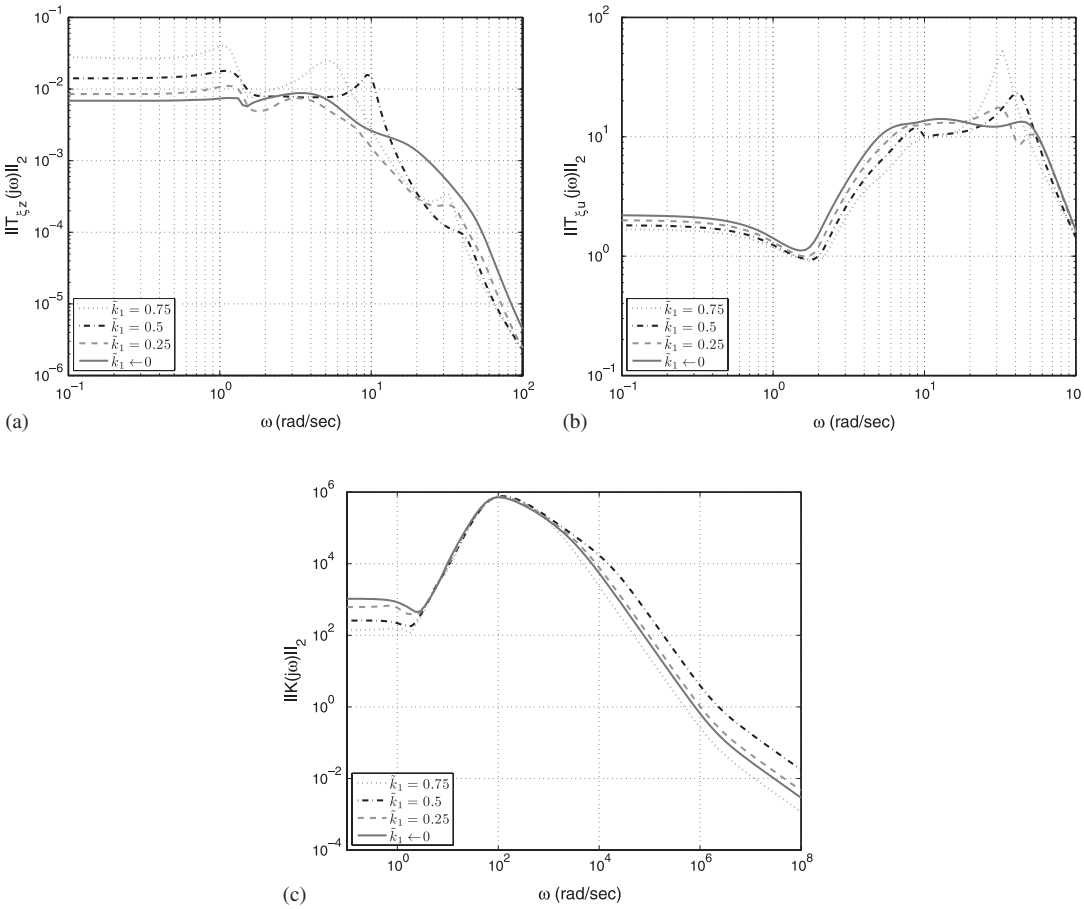

Figure 14. Maximum singular value (only k_1 uncertain, $A_2 = 5A_1$): (a) $T_{\xi z}(s)$; (b) $T_{\xi u}(s)$; and (c) $K(s)$.

defined in (20), the control has most of its power located at the frequency range $\omega \in [0 \;\; 10^6]$ rad/s. The poles located near the frequency $\omega = 10^2$ rad/s cut the compensator bandwidth, where the zero of $\mathbf{W}_{pu}(s)$ starts to penalize the control signal, to finally attenuate the control signal power for $\omega > 10^6$ rad/s. The control gain in Figure 12(c) is large because it translates position error to force, but the order of magnitude of the control inputs and the disturbances is the same, as it will be illustrated by the results of the time simulations. Also, the control gain can be shaped to satisfy control input limitations, at the price of degrading disturbance-rejection.

The maximum singular value plots for $A_1 = 5A_2$ and $A_2 = 5A_1$ bear the same characteristics described for $A_1 = A_2$, see Figures 13 and 14. The closed-loop directionality is illustrated properly by the SVD plots, presented in the sequel.

For the two uncertain parameter case, the stability- and performance-robustness characteristics described in the single uncertainty case also apply. In particular, Figure 15 depicts the disturbance-rejection and compensator transfer function for fixed $\tilde{k}_1$ and varying $\tilde{m}_3$.

DOI: 10.1002/rnc

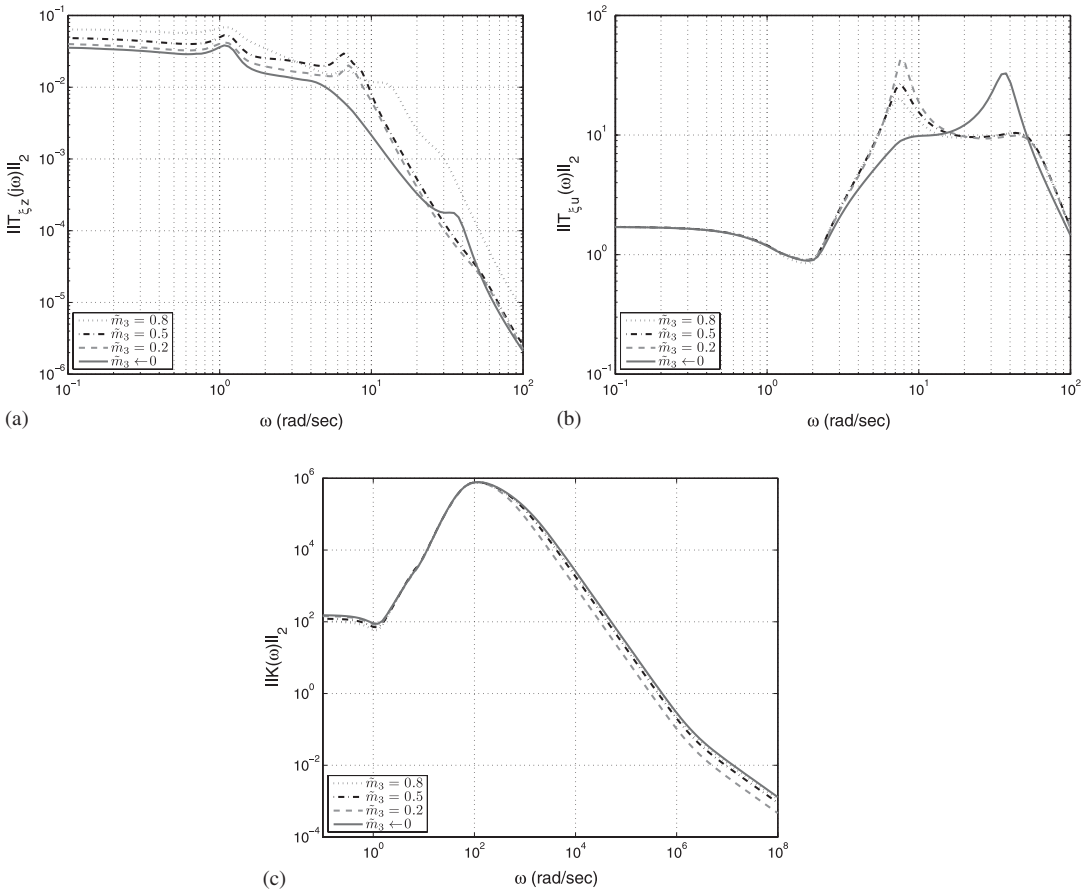

Figure 15. Maximum singular value (k_1, m_3 uncertain, $\tilde{k}_1 = 0.75$, $A_1 = A_2$): (a) $T_{\xi z}(s)$; (b) $T_{\xi u}(s)$; and (c) $K(s)$.

The directionality of the system can be analyzed from Figure 16. The gap between the maximum and minimum singular values changes significantly as we change the uncertainty levels. This implies that the directional properties (dynamic coupling) of the robust multivariable design are significantly influenced by the parameter uncertainty levels. The performance vectors $z_1(t)$ and $z_2(t)$ tend to be equally influenced by the disturbance when the performance weights are similar ($A_1 = A_2$), see Figure 16(d). Figure 16 also shows that changes in system performance robustness are more influenced by the elastic coefficient uncertainty $\tilde{k}_1$ than by the mass 3 uncertainty $\tilde{m}_3$, when $A_1 = A_2$.

In the case where the frequency weights introduce additional directionality, $A_1 = 5A_2$ or $A_2 = 5A_1$, the maximum singular value is approximately five times the value of the minimum singular value, as shown in Figures 17 and 18.

Note that in the case $A_1 = 5A_2$, the closed-loop disturbance-rejection SVD plot with uncertainty in m_3 and $\tilde{k}_1 \approx 0$ is very similar to the SVD plot with $\tilde{m}_3 \approx 0, \tilde{k}_1 \approx 0$, depicted in Figures 17(b) and (d), respectively. Also, reducing the mass m_3 uncertainty has little impact on the $T_{\xi z}(s)$

DOI: 10.1002/rnc

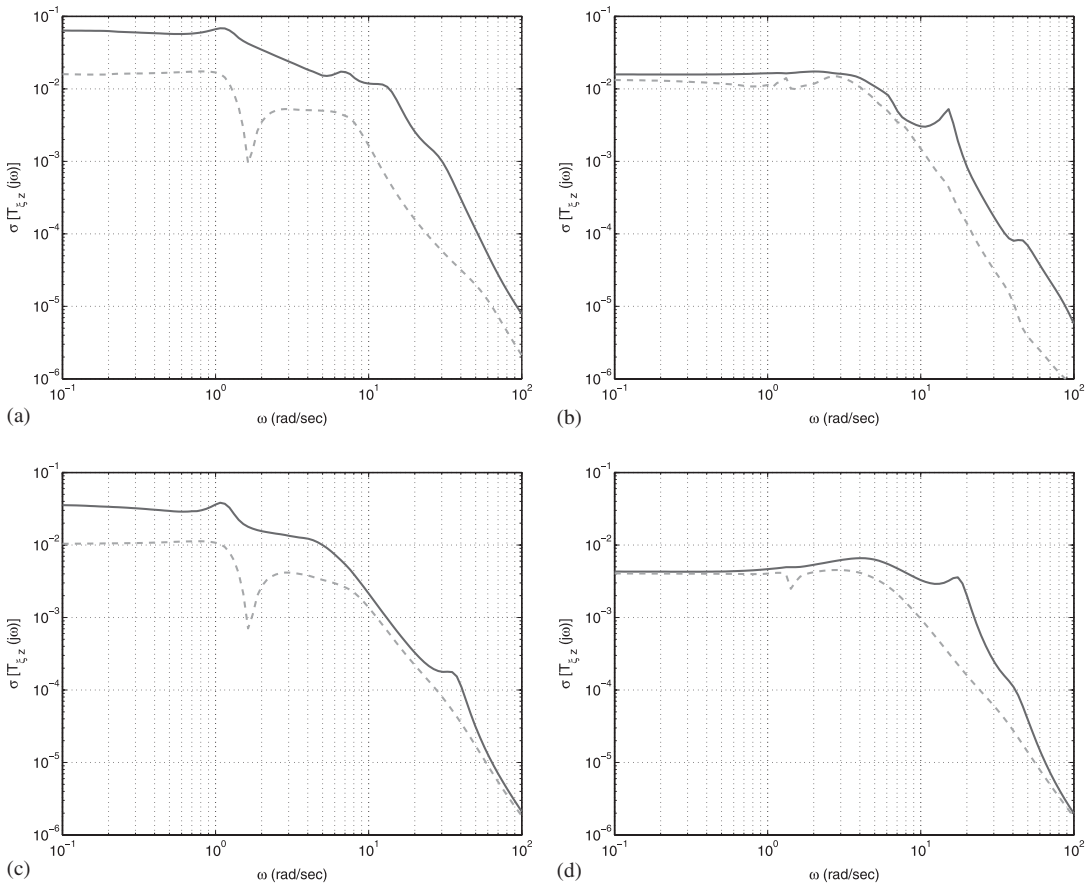

Figure 16. Closed-loop $T_{\xi z}(s)$ singular values (k_1, m_3 uncertain, $A_1 = A_2$): (a) $\tilde{m}_3 = 0.80, \tilde{k}_1 = 0.75$; (b) $\tilde{m}_3 = 0.80$, $\tilde{k}_1 \approx 0$; (c) $\tilde{m}_3 \approx 0, \tilde{k}_1 = 0.75$; and (d) $\tilde{m}_3 \approx 0, \tilde{k}_1 \approx 0$.

directionality for $A_1 = 5A_2$; compare Figures 17(a) with (c). This indicates that the spring stiffness k_1 is an important parameter in the control of mass 2 position. The converse occurs with mass m_3 in the control of mass 3, as illustrated by Figure 18, which illustrates the existing subsystems of the MSD plant.

The superiority of the mixed-μ synthesis over the complex-μ one is evident in Figures 19 and 20. The disturbance-rejection and the controller transfer functions are more conservative for the compensator obtained by the complex-μ method using the D-K iterations.

The frequency-domain results are in agreement with the performance results previously presented, and show that:

- The closed-loop plant indeed has superior disturbance-rejection over the frequency band where the plant disturbance $\mathbf{d}(s)$ has more power, so as to meet the designer-posed performance specifications.

DOI: 10.1002/rnc

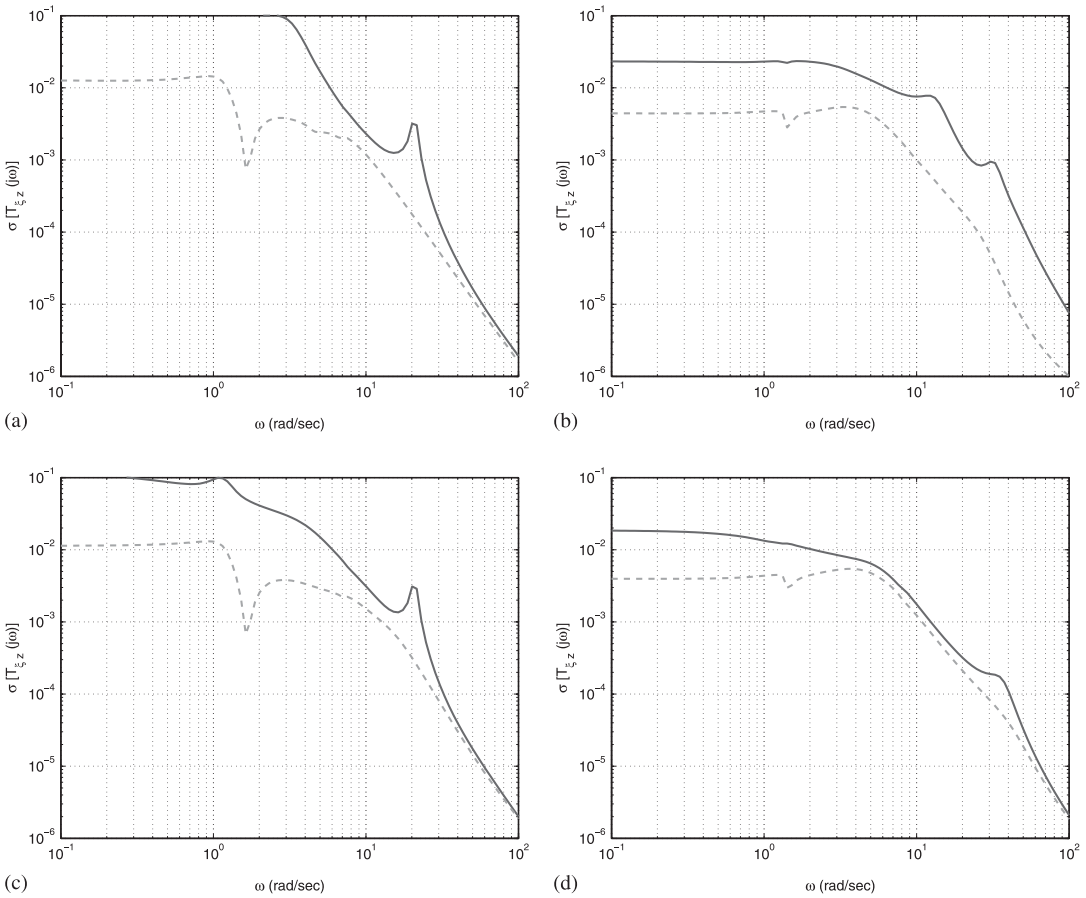

Figure 17. Closed-loop $T_{\xi z}(s)$ singular values (k_1, m_3 uncertain, $A_1 = 5A_2$): (a) $\tilde{m}_3 = 0.80, \tilde{k}_1 = 0.75$; (b) $\tilde{m}_3 = 0.80, \tilde{k}_1 \approx 0$; (c) $\tilde{m}_3 \approx 0, \tilde{k}_1 = 0.75$; and (d) $\tilde{m}_3 \approx 0, \tilde{k}_1 \approx 0$.

- The disturbance-rejection obtained by the D,G-K iterations is clearly superior than the one obtained by the D-K iterations in the low frequency, i.e. where $\mathbf{d}(s)$ has more power. These results are in agreement with those presented for performance robustness, which shows the importance of mixed-μ design to obtain better performance robustness at the relevant frequency regions, as compared with the complex-μ design.
- The directionality of the performance frequency weights shows that k_1 is more important in the control of mass 2, whereas m_3 is more relevant for the control of mass 3. The directionality properties (dynamic coupling) change significantly as the level of parametric uncertainty changes. The influence of the performance frequency weights A_1 and A_2 on the guaranteed stability- and performance-robustness also illustrates the interactions of the subsystems, from control inputs u_1 and u_2 to the position of masses 2 and 3, respectively.

DOI: 10.1002/rnc

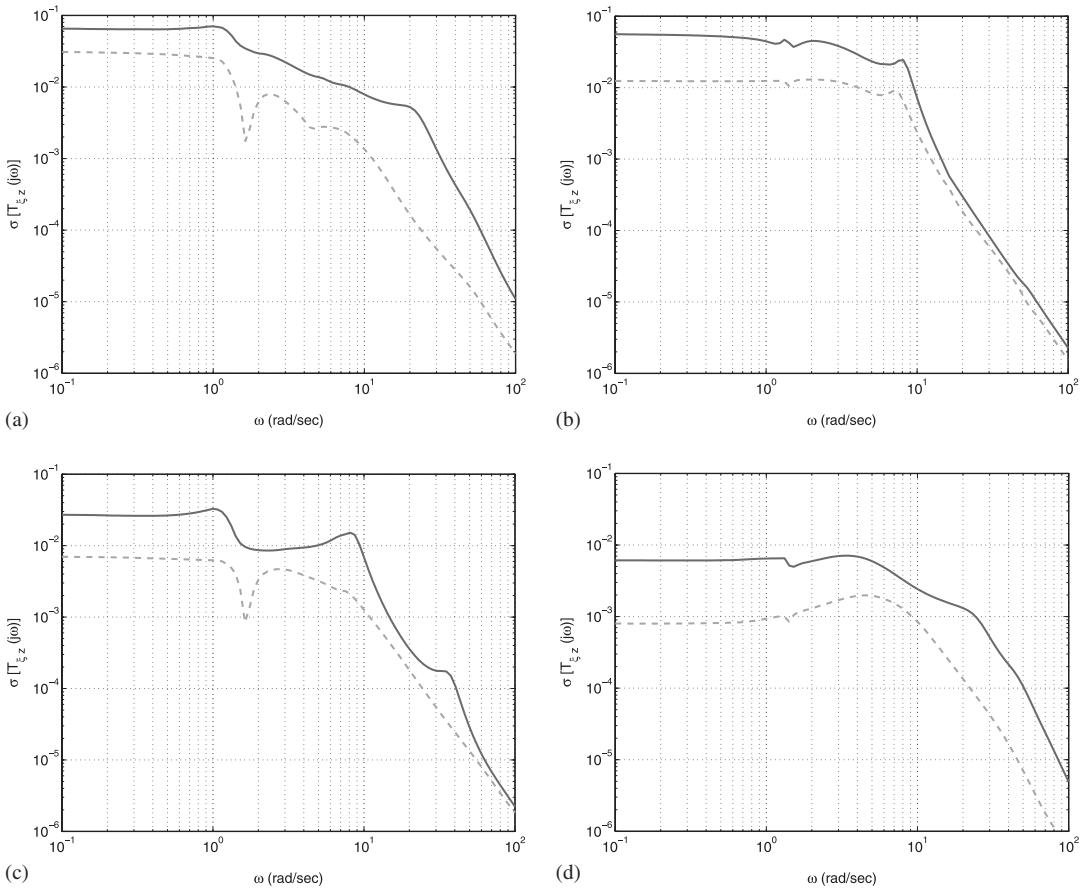

Figure 18. Closed-loop $T_{\tilde{\xi}z}(s)$ singular values (k_1, m_3 uncertain, $A_2 = 5A_1$): (a) $\tilde{m}_3 = 0.80, \tilde{k}_1 = 0.75$; (b) $\tilde{m}_3 = 0.80, \tilde{k}_1 \approx 0$; (c) $\tilde{m}_3 \approx 0, \tilde{k}_1 = 0.75$; and (d) $\tilde{m}_3 \approx 0, \tilde{k}_1 \approx 0$.

- The maximum and minimum singular values ratio, and hence the closed-loop directionality, is also determined by the performance weights A_1 and A_2 ratio, focusing the control problem on the mass 2 or 3 position errors, respectively.

6. TIME-DOMAIN SIMULATIONS

In this section, we present some time simulations for the mixed-μ designs. First, in order to obtain a precise feeling of the directionality properties, we use the SVD to generate the 'worst-case' disturbances associated with the maximum singular value direction. Next a filtered square-wave disturbance is applied to the system to analyze the dynamics of the plant output's time response.

The time-domain simulations for sinusoidal disturbances corresponding to maximum disturbance amplification are presented in Figure 21. The 'worst-case' unit disturbances $d_1(t)$ and $d_2(t)$ act in phase with positions $x_2(t)$ and $x_3(t)$. The control signals $u_1(t)$ and $u_2(t)$ have a 180° phase shift

DOI: 10.1002/rnc

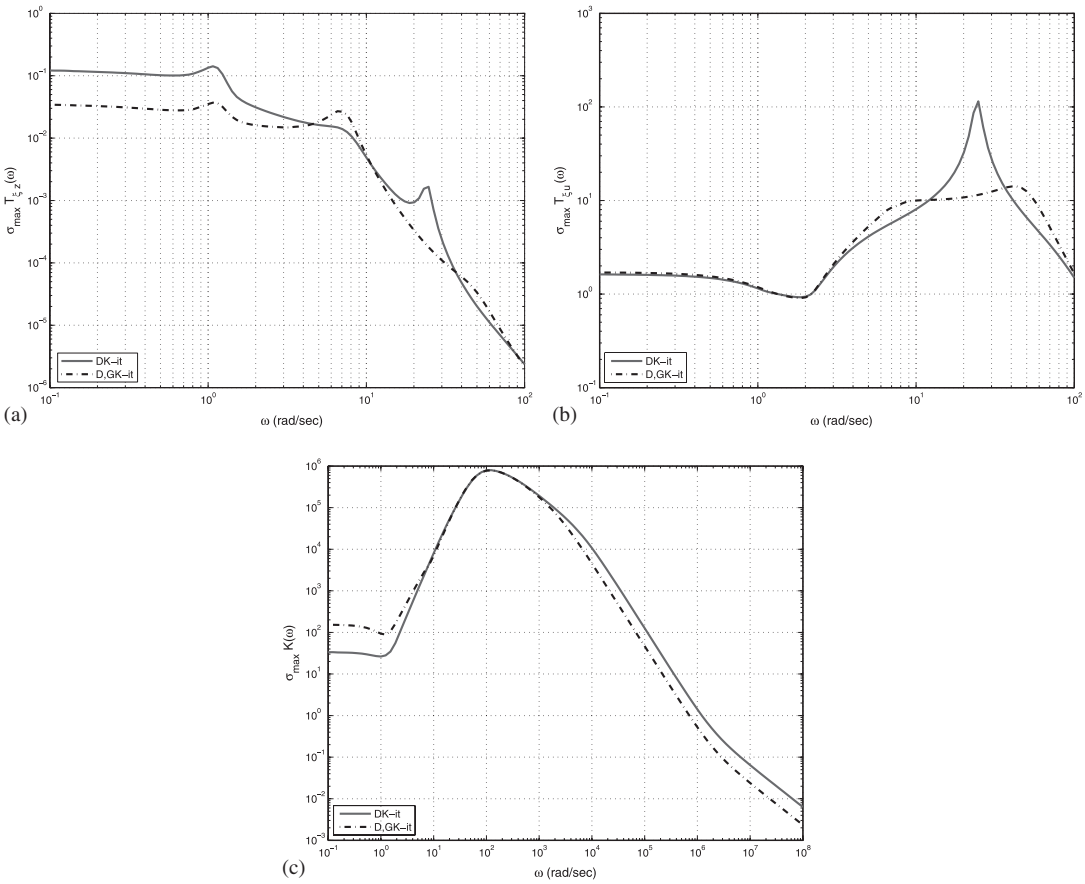

Figure 19. D-K iteration (complex-μ) *vs* D,G-K iteration (mixed-μ) maximum singular value (only k_1 uncertain, $\tilde{k}_1 = 0.75$, $A_1 = A_2$): (a) $T_{\xi z}(s)$; (b) $T_{\xi u}(s)$; and (c) $K(s)$.

with respect to the disturbances to counteract their effect, as expected, and the order of magnitude of the control input and the disturbances is the same. For $A_1 = 5A_2$, the $z_2(t)$ performance output amplitude is larger than $z_1(t)$, since the first one is cheaper than the latter, see Figure 21(b). The converse occurs for $A_2 = 5A_1$ as shown in Figure 21(c). These plots illustrate in a concrete way how the directionality properties change.

The generalized plant, shown in Figure 7, is simulated to study the effects of unmodeled state disturbance in the system. It is assumed that the real control delay is $\tau_1 = \tau_2 = 5 \times 10^{-3}$ s and that the uncertain parameters are given by the nominal values $k_1 = \bar{k}_1, m_3 = \bar{m}_3$.

Applying a filtered square-wave signal $\boldsymbol{\xi}(t)$ produces disturbance $\mathbf{d}(t)$ depicted in Figure 22 and yields the mass displacements shown in Figure 23. This particular disturbance was selected so that it would 'sweep' across the different disturbance directions. Clearly, the smaller the uncertainty, the better the time response of the system, i.e the better the disturbance-rejection. The control input $u_1(t)$ counteracts the effects of $d_1(t)$, whereas $u_2(t)$ is influenced by the sign of $(d_1(t) - d_2(t))$,

DOI: 10.1002/rnc

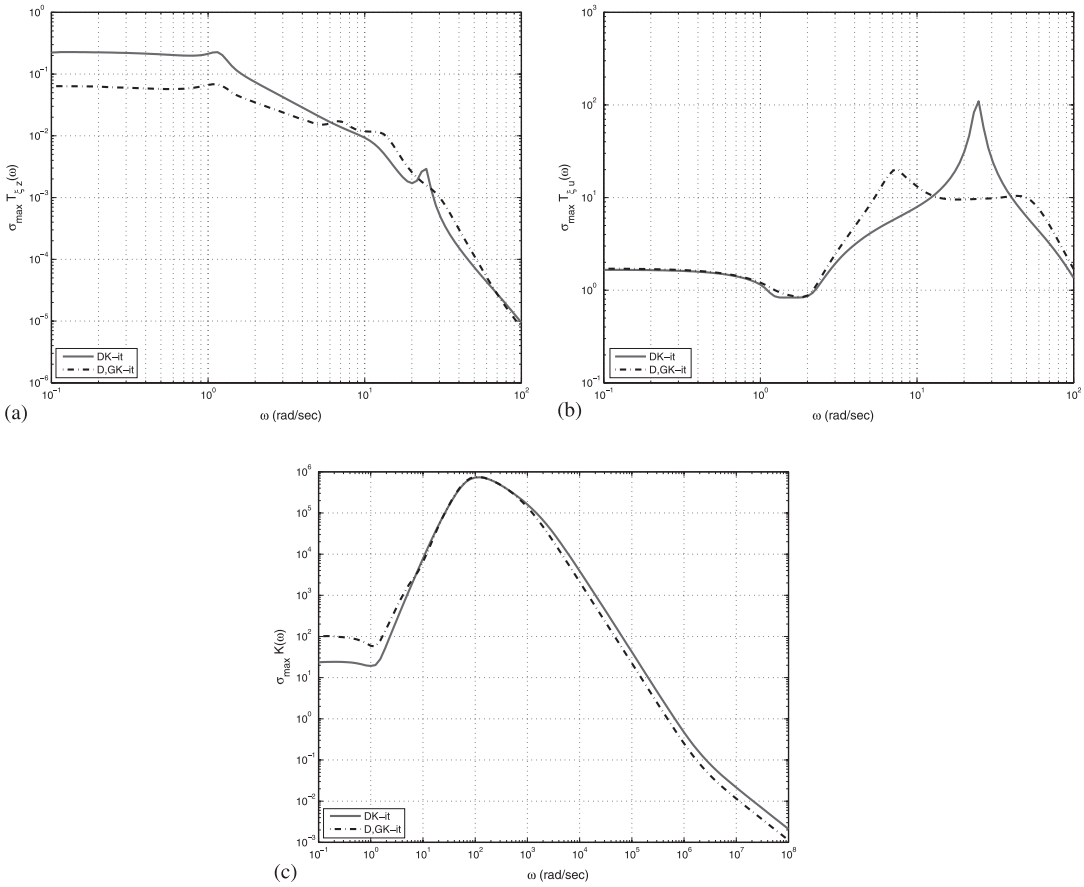

Figure 20. D-K iteration (complex-μ) *vs* D,G-K iteration (mixed-μ) maximum singular value (k_1, m_3 uncertain, $\tilde{k}_1 = 0.75$, $\tilde{m}_3 = 0.8$, $A_1 = A_2$): (a) $T_{\xi z}(s)$; (b) $T_{\xi u}(s)$; and (c) $K(s)$.

as depicted in Figure 24. The time-domain results are in agreement with the frequency-domain results discussed in Section 5.

7. STABILITY REGIONS FOR LEGAL UNMODELED DYNAMICS

In this section, the actual closed-loop stability of the system is studied and compared with the stability- and performance-robustness region guaranteed by the mixed-μ synthesis. Performance-robustness specifications are neglected to study how closed-loop stability is extended outside the nominal stability and performance bounds $(\delta_{k_1}, \delta_{m_3}) < 1$. The difference between the nominal and the actual stability regions is referred to as the stability margin.

The technique to model the pure time-delay error $e_M(s)$ using a high-pass frequency weight $\mathbf{W}_\tau(s)$, depicted in Figure 4, is a common but conservative approach. As we have remarked before, the error magnitude envelope $\|\mathbf{W}_\tau(s)\mathbf{\Delta}_\tau(s)\|$ accounts for a generic set of unmodeled dynamics,

DOI: 10.1002/rnc

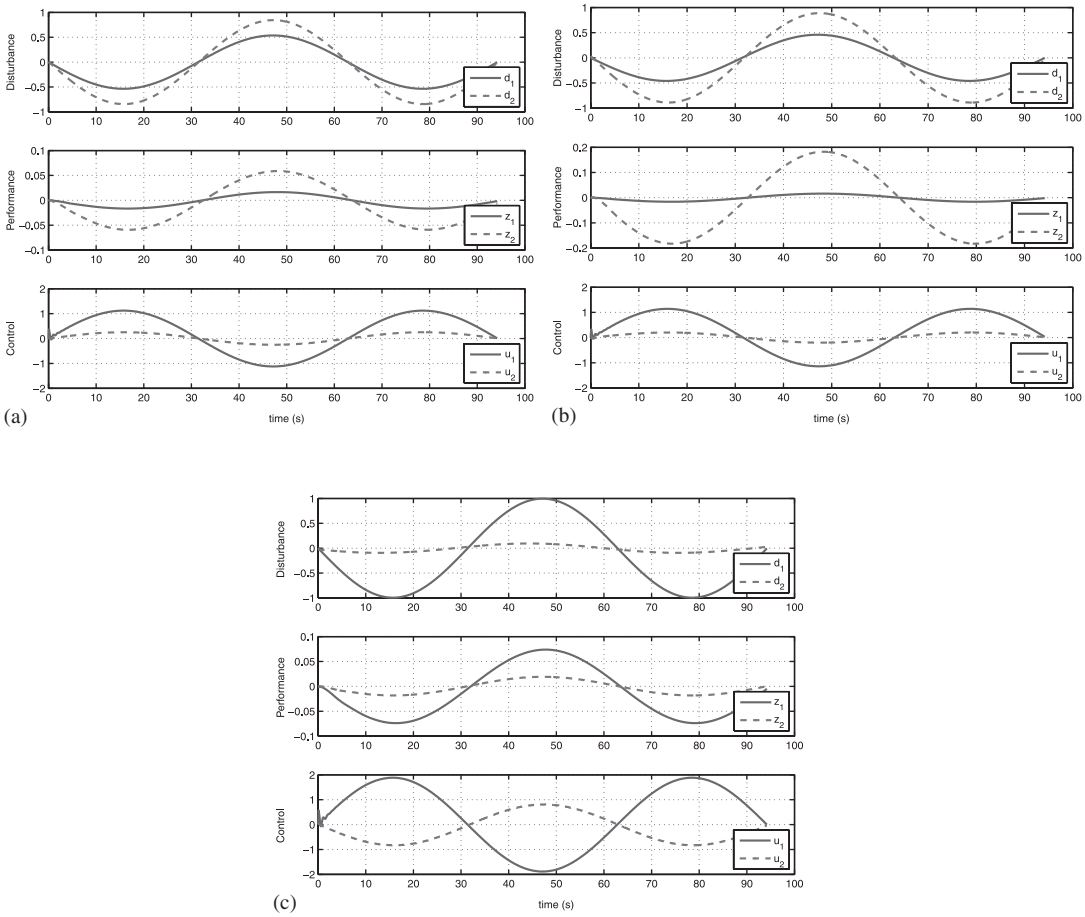

Figure 21. Maximum singular value sinusoidal disturbance (k_1, m_3 uncertain, $\tilde{k}_1 = 0.75, \tilde{m}_3 = 0.80$): (a) $A_1 = A_2$; (b) $A_1 = 5A_2$; and (c) $A_2 = 5A_1$.

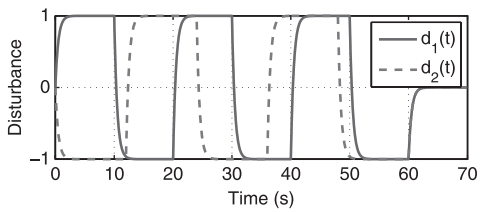

Figure 22. Filtered square-wave disturbance.

of which the pure time-delay error $e_M(s)$ is just one particular point. We analyze the closed-loop stability margins for (i) a pure time-delay Padé approximation and (ii) the worst legal $\mathbf{\Delta}_\tau(s)$ that destabilizes the system.

DOI: 10.1002/rnc

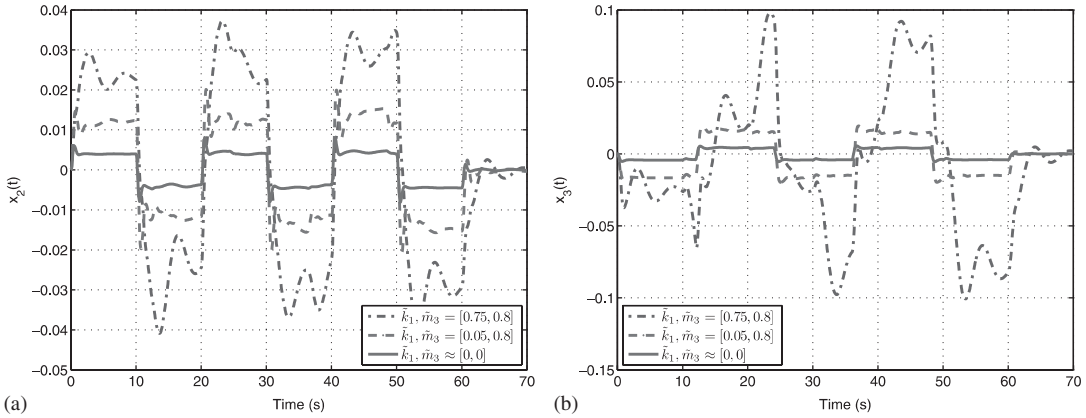

Figure 23. Mass positions (filtered square-wave disturbance, $A_1 = A_2$): (a) mass 2 position and (b) mass 3 position.

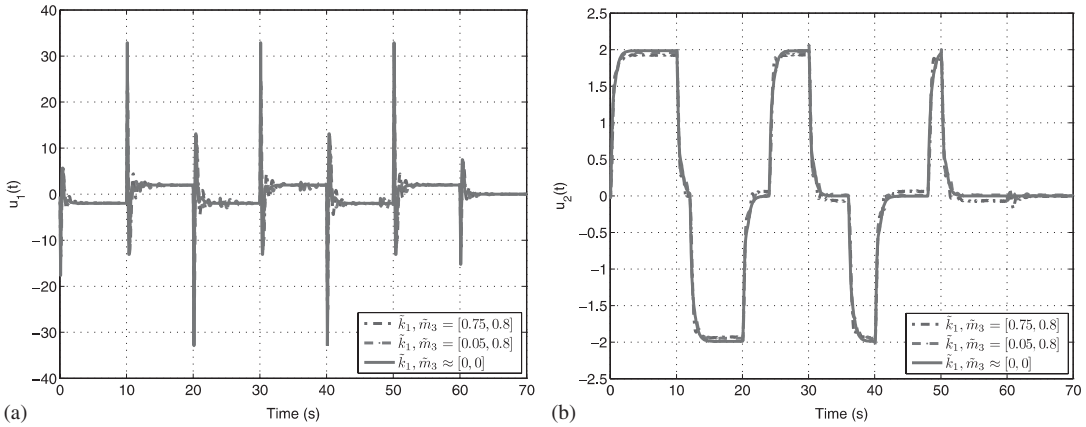

Figure 24. Control inputs (filtered square-wave disturbance, $A_1 = A_2$) applied to: (a) mass 1 and (b) mass 3.

7.1. Unmodeled time delay

To compute the actual plant stability region, the time-delay error model is replaced by a sixth-order Padé approximation;[¶] hence, we can check the closed-loop stability using eigenvalues rather than the multivariable Nyquist criterion. Because the time delay is only one of the legal disturbances admitted by the upper bound $\|\mathbf{W}_\tau(s)\|$, the stability-only region of the closed-loop plant is larger than the nominal stability- and performance-robustness region, as shown in Figure 25. Note that for the nominal design, Figure 25(a), the system becomes unstable for hard spring stiffness k_1 and

[¶]The Padé approximation order was limited by the computational accuracy of the MATLAB software.

DOI: 10.1002/rnc

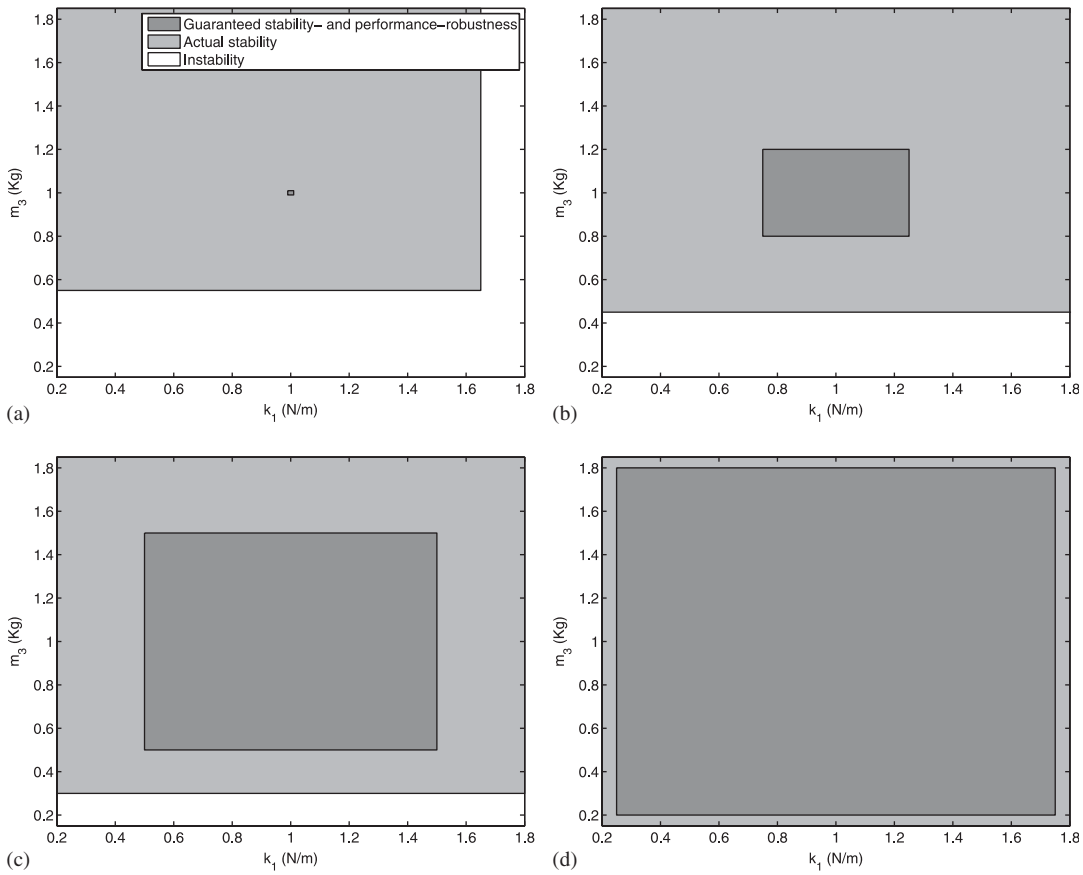

Figure 25. Actual and mixed-μ guaranteed stability regions, (Padé approximation, $A_1 = A_2$): (a) $\tilde{k}_1 \approx 0$, $\tilde{m}_3 \approx 0$ compensator; (b) $\tilde{k}_1 = 0.25$, $\tilde{m}_3 = 0.20$ compensator; (c) $\tilde{k}_1 = 0.50$, $\tilde{m}_3 = 0.50$ compensator; and (d) $\tilde{k}_1 = 0.80$, $\tilde{m}_3 = 0.75$ compensator.

light mass m_3. The actual stability region increases when we use the robust compensators, see Figures 25(b)–(d).

The closed-loop disturbance-rejection $T_{\xi z}(s)$ singular value plots for the nominal point $(m_3, k_1) = (1, 1)$ and for a stable point $(m_3, k_1) = (0.55, 1.65)$, which is close to the instability region (see Figure 25(a)), are shown in Figures 26 and 27, respectively. The disturbance-rejection properties of the compensator designed for large uncertainties are very similar, see Figures 26(a) and 27(a), which evidences the closed-loop performance robustness. The performance of the compensator designed for very small uncertainties degrades at the almost unstable point, see Figures 26(b) and 27(b).

The interesting point is to compare the disturbance-rejection plots of Figure 27. From a pure $\mathscr{H}_\infty$ perspective, the nominal design, resulting in Figure 27(b), is not robust because at about $\omega = 18$ rad/s its $\mathscr{H}_\infty$ norm is larger than that of the robust design of Figure 27(a). However, for the frequency region of interest, $\omega \in [0\ \ 2]$ rad/s, the 'non-robust nominal design' associated

DOI: 10.1002/rnc

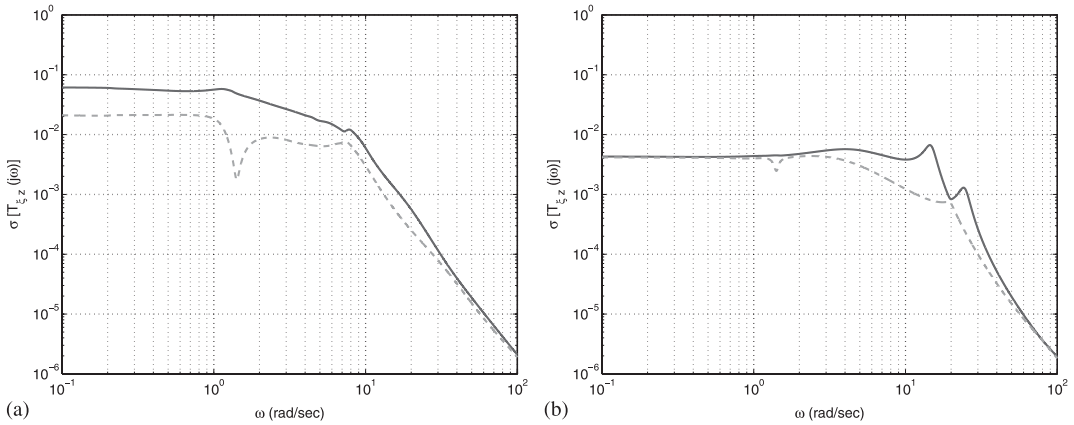

Figure 26. $T_{\xi z}(s)$ for $(m_3, k_1) = (1, 1)$ $(A_1 = A_2)$: (a) compensator for $k_1 \in (0.25, 1.75)$, $m_3 \in (0.20, 1.80)$ and (b) compensator for $k_1 \approx 1$, $m_3 \approx 1$.

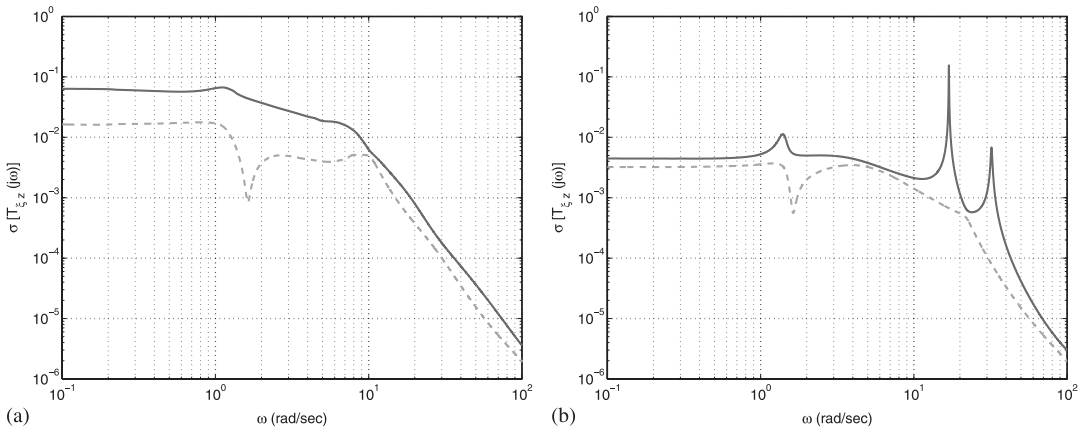

Figure 27. $T_{\xi z}(s)$ for $(m_3, k_1) = (0.55, 1.65)$, (Padé approximation, $A_1 = A_2$): (a) compensator for $k_1 \in (0.25, 1.75)$, $m_3 \in (0.20, 1.80)$ and (b) compensator for $k_1 \approx 1$, $m_3 \approx 1$.

with Figure 27(b) yields better disturbance-rejection than the 'robust design' of Figure 27(a) in all directions. This demonstrates that one should be careful in comparing robust *vs* non-robust designs using only the $\mathscr{H}_\infty$ metric; it is best to compare them over the entire frequency range as in Figure 27. Since μ-synthesis always yields $\mathscr{H}_\infty$ compensators, such comparisons are important from an engineering perspective.

7.2. Worst-case unmodeled dynamics

We were surprised at the large stability region associated with the nominal design shown in Figure 25(a). This led us to investigate similar issues for other 'legal' unmodeled dynamics.

DOI: 10.1002/rnc

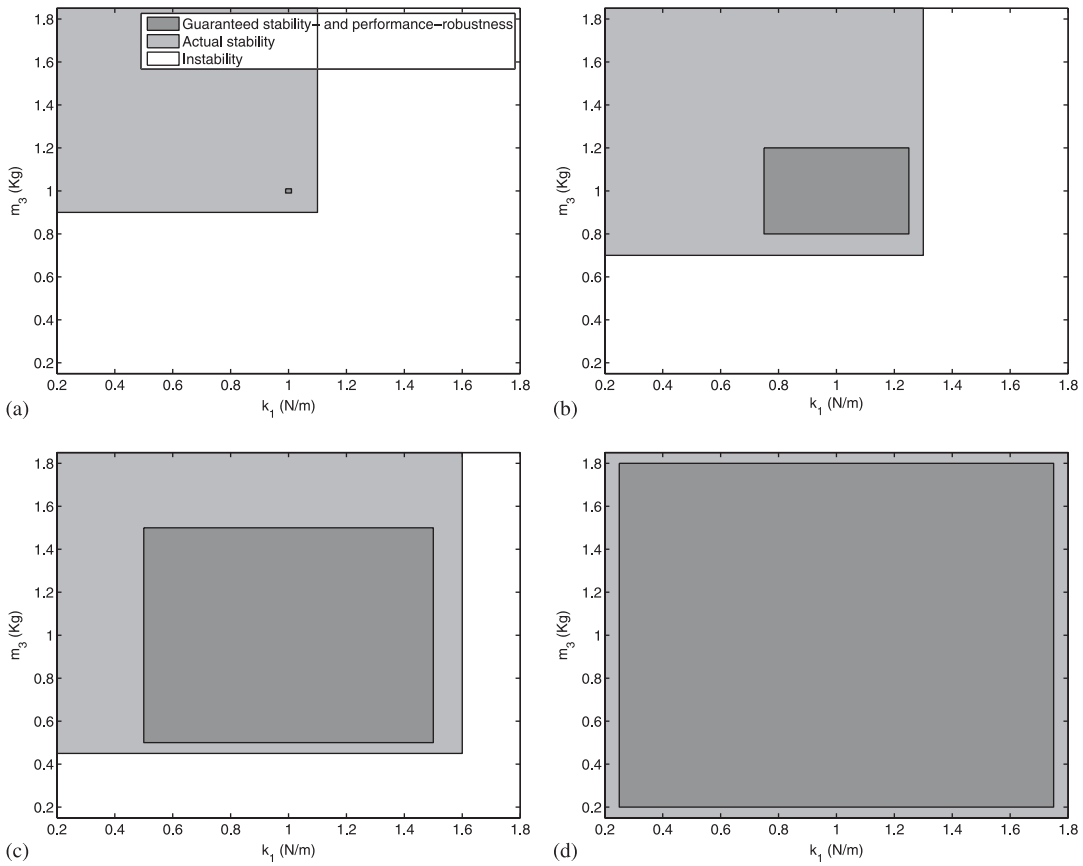

Figure 28. Actual and mixed-μ guaranteed stability regions ($\Delta_\tau(s)$ approximation, $A_1 = A_2$): (a) $\tilde{k}_1 \approx 0$, $\tilde{m}_3 \approx 0$ compensator; (b) $\tilde{k}_1 = 0.25$, $\tilde{m}_3 = 0.20$ compensator; (c) $\tilde{k}_1 = 0.50$, $\tilde{m}_3 = 0.50$ compensator; and (d) $\tilde{k}_1 = 0.80$, $\tilde{m}_3 = 0.75$ compensator.

According to the stability specifications, the mixed-μ compensator guarantees closed-loop stability for any time delay with $\tau \leqslant 0.03$ s and also for *any* uncertainty whose magnitude is below the envelope $\|\mathbf{W}_\tau(s)\|$. Instead of using the particular Padé approximation, the stability margins are computed for the worst-case destabilizing $\mathbf{\Delta}_\tau(s)$.

The stability of the closed-loop system is determined by the μ bounds. For each point (k_1, m_3), the system is stable if the μ upper bound is smaller than unity, $\bar{\mu} < 1$, or unstable if the μ lower bound is bigger than unity, $\underline{\mu} > 1$. If none of them is verified, then the stability of the system cannot be determined using the μ tools. The destabilizing delta, associated with the μ lower bound, is easily constructed using the command `dypert` included in the MATLAB Robust Toolbox [3].

The stability-only region for the worst destabilizing delta $\mathbf{\Delta}_\tau(s)$, depicted in Figure 28, is closer to the nominal stability- and performance-robustness limits obtained in the μ-synthesis design. Since the stability is analyzed independent of performance specifications [22], the stability-only region of the closed-loop is still larger than the region where, both stability and performance are guaranteed.

DOI: 10.1002/rnc

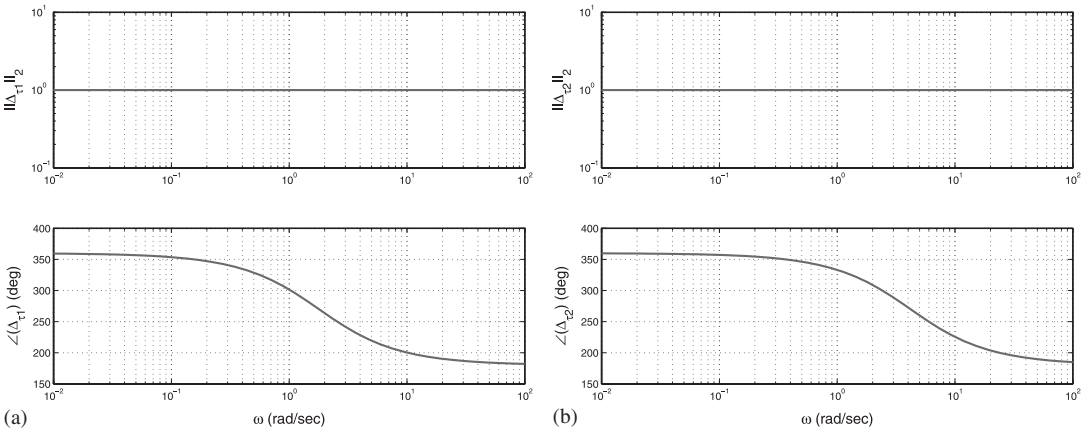

Figure 29. Bode plots of destabilizing legal delta $\mathbf{\Delta}_\tau(s)$ for $(m_3, k_1) = (0.90, 1.15)$: (a) $\Delta_{\tau 1}(s)$ and (b) $\Delta_{\tau 2}(s)$.

For the stability region boundary point $(m_3, k_1) = (0.90, 1.15)$, the transfer function of the destabilizing delta, depicted in Figure 29, is given by

$$\begin{aligned} \Delta_{\tau 1}(s) &= \frac{-s^2 - 2.40s + 7.49}{s^2 + 5.98s + 7.49} = -\frac{(s+4.19)(s-1.79)}{(s+4.19)(s+1.79)} \\ \Delta_{\tau 2}(s) &= \frac{-s^2 + 2.40s + 7.49}{s^2 + 5.98s + 7.49} = -\frac{(s-4.19)(s+1.79)}{(s+4.19)(s+1.79)} \end{aligned} \tag{21}$$

where the order of the canceling pole and minimum phase zero difference is of the order of MATLAB's numerical precision. The difference between the $\Delta_{\tau 1}(s)$ and $\Delta_{\tau 2}(s)$ transfer functions illustrates an additional interesting directionality property of the closed-loop plant.

As illustrated by (21), the legal $\mathbf{\Delta}_\tau(s)$ that destabilize the closed-loop plant yield a transfer function $\mathbf{I} + \mathbf{W}_\tau(s)\mathbf{\Delta}_\tau(s)$, which does not represent a time delay. The different stability margins for the Padé approximation and for the worst destabilizing delta, Figures 25 and 28, show that the stability-robustness specifications for the time delay are conservative: the time delay is not always a destabilizing delta. Thus, the worst destabilizing delta $\mathbf{\Delta}_\tau(s)$ (21) results in the much smaller closed-loop stability regions of Figure 28 compared with those of Figure 25. Consequently, the obtained stability margins are due more to the conservative time-delay model than to the controller synthesis method. Intuitively, one can argue that the maximum time-delay does not 'point' towards the worst destabilizing direction while (21) does.

The performance of the nominal $(\tilde{k}_1, \tilde{m}_3) \approx (0, 0)$ compensator degrades in the stability-only region, as shown in Figure 30. By comparing Figures 27 and 30, we see similar behavior. For the nominal design performance degradation occurs at high frequencies, while obtaining better disturbance-rejection in the desired low-frequency region. Either using the Padé approximation or the destabilizing delta, the fact that performance degradation occurs after the corner frequency $\alpha = 2$ rad/s is not negligible and may very well be acceptable for practical implementation. Nonetheless, from the point of view of $\mathscr{H}_\infty$ norm minimization, the disturbance to output norm is effectively degraded.

DOI: 10.1002/rnc

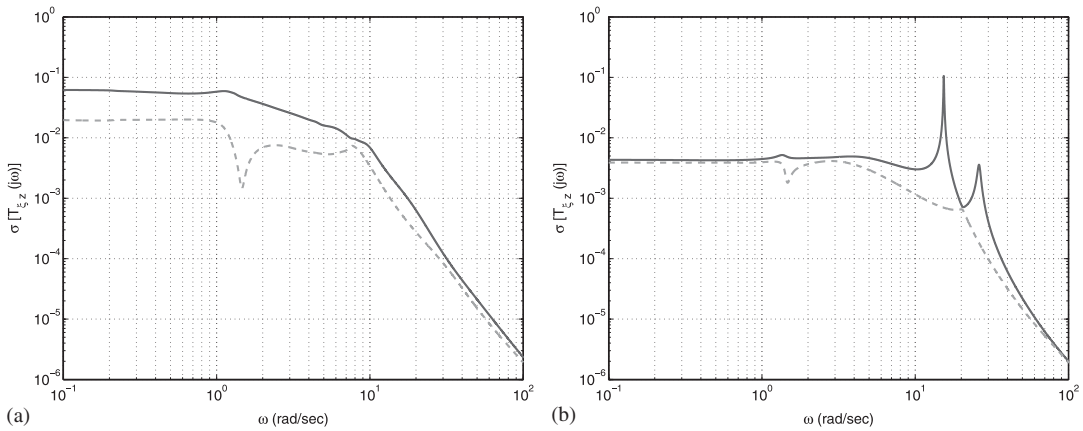

Figure 30. $T_{\tilde{\xi}z}(s)$ for $(m_3, k_1) = (0.90, 1.13)$ $(A_1 = A_2)$: (a) compensator for $k_1 \in (0.25, 1.75)$, $m_3 \in (0.20, 1.80)$ and (b) compensator for $k_1 \approx 1$, $m_3 \approx 1$.

The stability margin results discussed above showed that we can extend stability by neglecting performance. The performance degradation at non-critical frequencies should be the subject for further research using other test examples and additional theory.

8. CONCLUSIONS

A robust compensator for a MSD plant with two parametric uncertainties was designed using the mixed-μ synthesis tools. The closed-loop transfer function was shaped by the compensator to meet the stability- and performance-robustness requirements in the frequency domain. It was observed that the mixed-μ synthesis compensator achieved good performance and stability robustness for the given plant.

Best performance and disturbance-rejection are obtained for smaller uncertainties, while very large uncertainties degrade the closed-loop performance. The directionality of the closed-loop transfer function is shaped by the performance weights. Also, performance weights show that mass 2 position is more difficult to control than mass 3 position, as expected from an engineering perspective.

The commercially available complex-μ D-K iterations yield very conservative performance for real parametric uncertainties. From the users' point of view, D-K and D,G-K software use the same configuration parameters, which makes mixed-μ highly appealing for robust controller synthesis.

The mixed-μ compensator is stable in a region outside the μ-bounds region if performance is neglected. The closed-loop is robust to modeling errors in the parametric uncertainties, at the cost of performance degradation. This demonstrates the tradeoff between stability and performance, which must always be considered in controller synthesis.

Some important questions arise for future work. The numerical results of Section 7 raise some important questions in performance robustness from an engineering perspective. Also, a deeper and general theoretical basis is required to study which uncertain real parameters are most relevant for μ-synthesis and how conservative is this design methodology.

DOI: 10.1002/rnc

ACKNOWLEDGEMENTS

This work was partially supported by Fundação para a Ciência e a Tecnologia (ISR/IST plurianual funding) through the POS_Conhecimento Program that includes FEDER funds. The work of J. F. Vasconcelos was supported by a PhD Student Scholarship from the Portuguese FCT POCTI programme (SFRH/BD/18954/2004).

REFERENCES

1. Skogestad S, Postlethwaite I. *Multivariable Feedback Control*: *Analysis and Design* (2nd edn). Wiley: New York, 2005.
2. Zhou K, Doyle JC. *Essentials of Robust Control*. Prentice-Hall: Englewood Cliffs, NJ, 1997.
3. Balas GJ, Doyle JC, Glover K, Packard A, Smith R. *μ-Analysis and Synthesis Toolbox*. The Mathworks, June 2004.
4. Wie B, Bernstein DS. Benchmark problems for robust control design. *Journal of Guidance*, *Control*, *and Dynamics* 1992; **15**(5):1057–1059.
5. Hergarten S, Jansen F. On the separation of timescales in spring–block earthquake models. *Nonlinear Processes in Geophysics* 2005; **12**:83–88.
6. Mitsui N, Hirahara K. Simple spring–mass model simulation of earthquake cycle along the Nankai Trough in southwest Japan. *Pure and Applied Geophysics* 2004; **161**(11–12):2433–2450.
7. Setareh M. Floor vibration control using semi-active tuned mass dampers. *Canadian Journal of Civil Engineering* 2002; **29**(1):76–84.
8. Kim SJ, Choi JW. Parametric uncertainty in controlling the vibration of a building. *Proceedings of the 39th SICE Annual Conference*, Iizuka, Japan, 2000; 107–112.
9. Nishimura H, Kojima A. Robust vibration isolation control for a multi-degree-of-freedom structure. *Proceedings of the 1998 IEEE Conference on Control Applications* (*CCA*), Trieste, Italy, September 1998.
10. Sun P-Y, Chen H. Multi-objective output-feedback suspension control on a half-car model. *Proceedings of the 2003 IEEE Conference on Control Applications* (*CCA*), vol. 1, Istanbul, Turkey, June 2003; 290–295.
11. Gaspar P, Szaszi I, Bokor J. Design of robust controllers for active vehicle suspension using the mixed μ synthesis. *Vehicle System Dynamics* 2003; **40**(4):193–228.
12. Burton AW, Truscott AJ, Wellstead PE. Analysis, modeling and control of an advanced automotive self-leveling suspension system. *IEE Proceedings. Control Theory and Applications* 1995; **142**:129–139.
13. Yamashita M, Fujimori K, Uhlik C, Kawatani R, Kimura H. H_∞ control of an automotive active suspension. *Proceedings on the 29th Conference on Decision and Control* (*CDC*), Honolulu, HI, December 1990.
14. Kienholz DA. Simulation of the zero-gravity environment for dynamic testing of structures. *Proceedings of the 19th Space Simulation Conference*, Baltimore, MD, October 1996.
15. Balas GJ, Young PM, Doyle JC. μ Based control design as applied to a large space structure: control design for the Minimast facility. *Technical Report*, NASA CSI/GI Final Report, 1992.
16. Chu PY, Wie B, Gretz B, Plescia C. Approach to large space structure control system design using traditional tools. *Journal of Guidance*, *Control*, *and Dynamics* 1990; **13**(5):874–880.
17. Campbell ME, Grocott S. Parametric uncertainty model for control design and analysis. *IEEE Transactions on Control Systems Technology* 1999; **7**(1):85–96.
18. How J, Glaese R, Grocott S, Miller D. Finite element model-based robust controllers for the Middeck active control experiment (MACE). *IEEE Transactions on Control Systems Technology* 1997; **5**(1):110–118.
19. How J, Hall SR, Haddad WM. Robust controllers for the Middeck active control experiment using Popov controller synthesis. *IEEE Transactions on Control Systems Technology* 1994; **2**(2):73–87.
20. Newlin MP, Young PM. Mixed μ problems and branch and bound techniques. *International Journal of Robust and Nonlinear Control* 1997; **7**:145–164.
21. Barros D, Fekri S, Athans M. Robust mixed-μ synthesis performance for a mass–spring benchmark system. *Proceedings of the 2005 IEEE International Symposium on Intelligent Control*, *Mediterranean Conference on Control and Automation*, Limassol, Cyprus, June 2005.
22. Balas GJ, Packard A. The structured singular value (μ) framework. *The Control Handbook*, Chapter 42. CRC Press: Boca Raton, FL, 1996; 671–687.
23. Stein G. Respect the unstable. *IEEE Control System Magazine* 2003; **23**(4):12–25.

DOI: 10.1002/rnc